Atomic-scale measurement of polar entropy

Debangshu Mukherjee ⬤,[1] Sergei Prokhorenko,[2,3] Leixin Miao,[1] Ke Wang,[4]
Eric Bousquet,[2] Venkatraman Gopalan,[1,4] and Nasim Alem[1,4,*]

[1]*Department of Materials Science and Engineering, The Pennsylvania State University, University Park, Pennsylvania 16802, USA*
[2]*Theoretical Materials Physics Q-MAT CESAM, University of Liège, Sart Tilman B-4000, Belgium*
[3]*Physics Department and Institute for Nanoscience and Engineering, University of Arkansas, Fayetteville, Arkansas 72701, USA*
[4]*Materials Characterization Laboratory, Materials Research Institute, The Pennsylvania State University,*
University Park, Pennsylvania 16802, USA

Entropy is a fundamental thermodynamic quantity that is a measure of the accessible microstates available to a system, with the stability of a system determined by the magnitude of the total entropy of the system. This is valid across truly mind boggling length scales, from nanoparticles to galaxies. However, quantitative measurements of entropy change using calorimetry are predominantly macroscopic, with direct atomic-scale measurements being exceedingly rare. Here, we experimentally quantify the polar configurational entropy (in meV/K) using sub-angstrom resolution aberration corrected scanning transmission electron microscopy in a single crystal of the prototypical ferroelectric $LiNbO_3$ through the quantification of the niobium and oxygen atom column deviations from their paraelectric positions. Significant excursions of the niobium-oxygen polar displacement away from its symmetry-constrained direction are seen in single domain regions which increase in the proximity of domain walls. Combined with first-principles theory plus mean field effective Hamiltonian methods, we demonstrate the variability in the polar order parameter, which is stabilized by an increase in the magnitude of the configurational entropy. This study presents a powerful tool to quantify entropy from atomic displacements and demonstrates its dominant role in local symmetry breaking at finite temperatures in classic, nominally Ising ferroelectrics.

I. INTRODUCTION

While absolute entropy, a fundamental thermodynamic parameter, is difficult to experimentally measure macroscopically, a change in entropy ($\Delta S = \frac{\Delta Q_{rev}}{T}$) is usually measured using calorimetry, where ΔQ_{rev} is the reversible heat supplied to the system at a constant temperature T [1,2]. At absolute zero ($T = 0$ K), the total entropy of a perfect crystal free of dopants is zero. Upon addition of reversible heat to the system, the entropy increases. Directly measuring the absolute entropy of the system through characterizing the microscopic configurations, or the microstates is challenging since it increases exponentially with the number of available microstates. Such enormously large numbers of microstates are also involved in condensed matter systems where a dopant atom may choose any one of equivalent atomic sites in a periodic lattice. The perturbation in atom positions from the crystal sites thus leads to an increase in the configurational entropy, which can be quantified through the probability distributions of the perturbations. Such configurational entropy may arise, for example, in ferroelectric crystals due to perturbations in the order parameter. The order parameter of a ferroelectric system is the spontaneous polarization, which arises as a consequence of the polar displacements [3]. The advances in aberration-

corrected scanning transmission electron microscopy (STEM) have now made it possible to quantify displacements with a precision approaching a single picometer [4–6], and even below a single picometer [7]. Recent results have demonstrated the feasibility of visualizing 2 pm magnitude charge density waves even at cryogenic temperatures with dark field STEM [8]. We build upon these advances to perform picometer precison quantification of polar displacements to quantify the variation in the order parameter in the well-known optical ferroelectric $LiNbO_3$ relative to its ideal ferroelectric structure. Throughout the rest of this work, we will refer to this entropy arising from the variability in polar displacements as polar entropy.

II. MEASUREMENT OF NIOBIUM-OXYGEN POLAR DISPLACEMENTS

Ferroelectric materials have a spontaneous and switchable electrical polarization, which is a consequence of the lattice distortions in the crystal structure that break inversion symmetry [9]. Regions of uniform polarization are called domains, with the boundary between two adjacent domains referred to as a domain wall [10,11]. Since the ferroelectric polarization is a consequence of crystal lattice distortions, the possible polar vectors can occur only along certain symmetry-allowed crystallographic directions. As a uniaxial displacive ferroelectric (space group *R3c*), the origin of the spontaneous

*alem@matse.psu.edu

polarization in $LiNbO_3$ is a consequence of the niobium and lithium cation displacements with respect to the oxygen octahedral center along either the (0001) or the (000$\bar{1}$) crystallographic axes, and thus the polarization vectors are restricted to only ⟨0001⟩ direction (also labeled as z or 3 direction) [12]. Classical uniaxial ferroelectrics such as $LiNbO_3$ have been long thought of as Ising type where the polarization is only along the two symmetry-restricted directions, which transitions to zero at the domain wall, since lattice distortions away from the symmetry-restricted polarization directions have a high-energy cost associated with them [13,14]. However, recent research has pointed out that fluctuations away from the Ising polarization direction do exist in other ferroelectrics, most notably $PbTiO_3$, with Bloch and Néel components arising at domain walls [15–18]. However, such deviations, as per the authors' knowledge, have never been observed before in $LiNbO_3$.

To visualize the atom positions at the 180° domain wall and also at the bulk domain, we imaged the electron transparent $LiNbO_3$ sample from the [1$\bar{1}$00] crystallographic zone axis so that the Ising displacements lie in plane. While both bright field (BF) and annular dark field (ADF) STEM images were acquired [Figs. 1(a) and 1(b)], we exclusively use BF-STEM images for the quantification of polar displacements since both the niobium and oxygen atom positions and their relative displacements can be quantified. This technique has been previously demonstrated as a viable pathway for the determination of the cation and oxygen atom positions simultaneously [19], and is less susceptible to specimen tilt and defocus in comparison to annular bright field (ABF) STEM [20,21]. The samples imaged in this experiment were approximately 25 nm thick, as determined from electron energy loss spectroscopy (EELS) inelastic mean-free path measurements (see Fig. 7 in Appendix A) [22].

The total polar displacements are calculated per unit cell, with respect to a mean unit cell calculated from the entire image [Fig. 1(c)]. The mean unit cell calculated from the STEM experimental data has the dimensions of 1390 pm × 259 pm, which is within 2% of the simulated $LiNbO_3$ $R3c$ unit-cell parameters of 1412.92 pm × 261.15 pm when viewed from the [1$\bar{1}$00] crystallographic zone axis [23]. As demonstrated in Fig. 1(d), displacements along ⟨0001⟩ are the Ising displacements, while those along ⟨11$\bar{2}$0⟩ are the Néel displacements. To determine the polar displacements, we first assigned the measured atom positions to their corresponding $LiNbO_3$ unit-cell positions, and then generated an average unit cell by summing all the individual unit cells throughout the BF-STEM image [Fig. 1(d)]. The oxygen and niobium centers of mass for each individual unit cell [Fig. 1(e)] were subsequently compared to the center of the calculated mean unit cell to determine the displacement vectors for both niobium and oxygen atoms for each $LiNbO_3$ unit cell imaged. The Nb-O polar displacement was then measured as a vector subtraction of the oxygen displacement vector from the niobium displacement vector. This calculated polar displacement vector was subsequently decomposed into its corresponding Ising and Néel components along the ⟨0001⟩ and ⟨11$\bar{2}$0⟩ directions, respectively, to obtain the individual polar components.

III. POLAR DISPLACEMENTS AT THE BULK DOMAIN AND THE DOMAIN WALL

Figure 2(a) demonstrates a section of the domain wall, with the scaled Ising displacements overlaid on the corresponding BF-STEM image. The blue regions refer to Ising displacements along the [000$\bar{1}$] axis, while the red regions indicate the Ising displacements along the [0001] direction. The 180° nature of the wall and the domain reversal across only one to two unit cells could be immediately ascertained, with the displacements being associated with simultaneous motion of both the niobium and the oxygen centers. Our measurements point to both oxygen and niobium atom columns displacing across the wall giving rise to a combined Ising displacement of 55 pm across the 180° domain wall as demonstrated in Fig. 2(a). Similar values for niobium displacements (≈25 pm) have been recently reported in $LiNbO_3$ through tracking the niobium atom columns with ADF-STEM [24]. In addition, the wall does not maintain a sharp atomic structure showing kinks and bends along itself as shown in Fig. 2(a). Figure 2(b) demonstrates that the domain wall and its proximity are also characterized by regions of Néel displacements, with parts of the wall featuring higher Néel intensities compared to the neighboring domain. In contrast to the Ising displacements, which are driven by the cooperative motion of oxygen and niobium atoms across the domain wall, the Néel displacements are, however, primarily driven by the niobium atoms reaching a maxima in absolute magnitude at the wall. We observe also that while the absolute magnitude of Néel displacements increase at the domain wall, Fig. 2(b) shows nonzero Néel displacements even inside the domain. Such non-Ising displacements have been predicted before at domain wall, though one may not expect them in a hard uniaxial ferroelectric [25]. Additionally, we observe that the maxima of the Néel displacements are not colocated with the center of the Ising displacements, as can be observed from Figure 2(d). This offset is due to the fact that the wall is not straight as indicated in Figs. 2(a) and 2(b). While the middle of the wall shows stronger Néel components, in the top half of the wall the Néel displacements die out due to the slight bending of the wall.

From the Ising and Néel displacements which we map in Figs. 2(a) and 2(b), respectively, it is obvious that contrary to the classical expectation of a pure Ising wall, non-Ising displacements do in fact occur. This is apparent as the magnitude of the curl increases at the wall Fig. 2(c)], indicating clockwise rotation of the polar niobium-oxygen displacement vectors. The Néel displacements, however, at the domain wall have a directional preference, which may be due to the higher electrostatic energy needed for head-to-head or tail-to-tail configurations arising from bidirectional Néel displacements. The electron microscope thus paints a picture of the 180° $LiNbO_3$ domain wall where the polar displacements demonstrate variation spatially, something that we observed consistently at other images of the domain wall too (Figs. 15–18), and even in images of the bulk domain (Figs. 13 and 14), indicating perturbations in the polar order parameter, and thus increased polar entropy at the wall.

To visualize the polar behavior away from the domain wall, we also imaged a section of the bulk domain, approximately 100 nm away from the domain wall in Figs. 3(a) and 3(b).
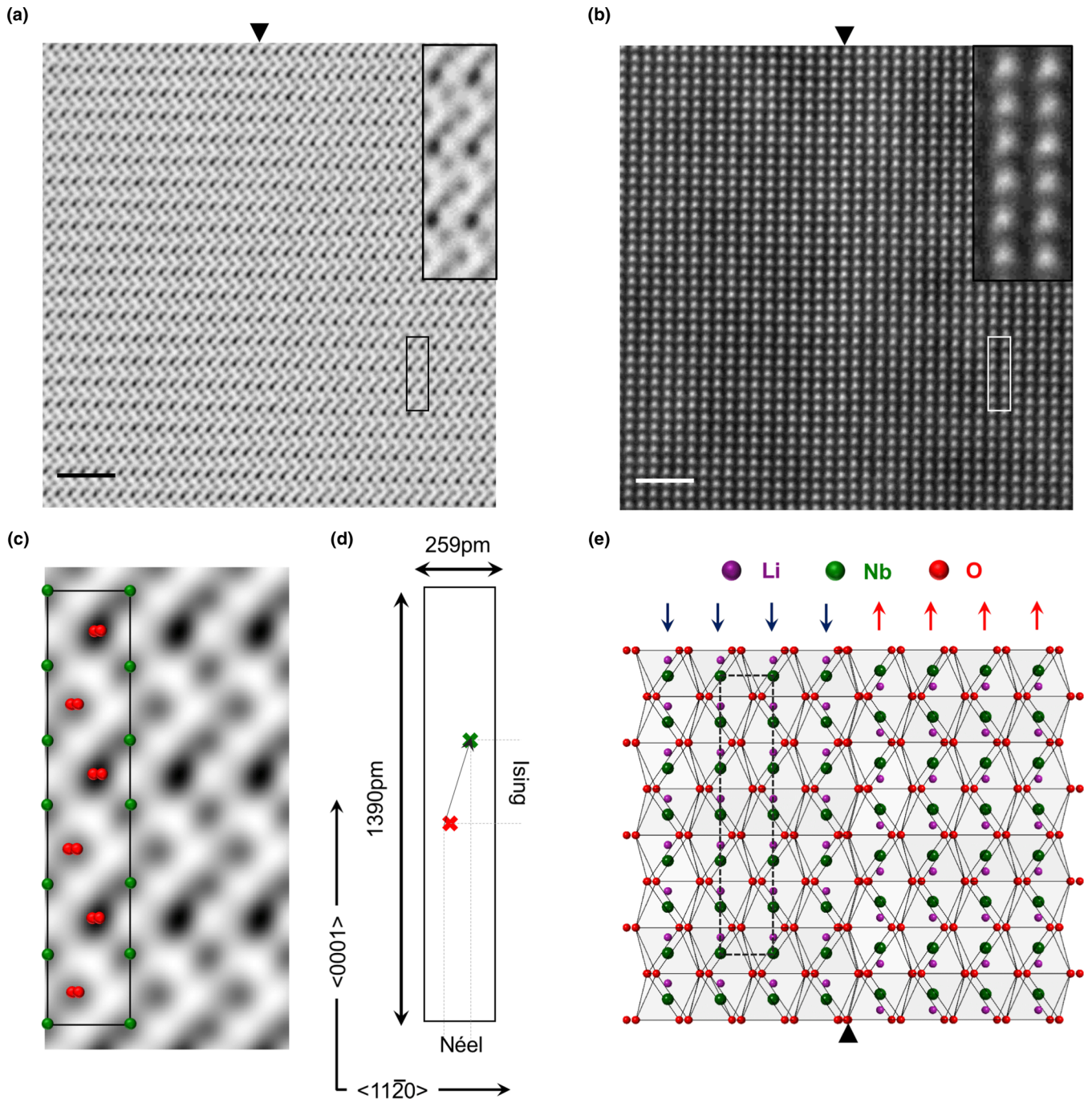
FIG. 1. Schematic of electron microscopy experiments. (a) Aberration-corrected BF-STEM image of a domain wall in LiNbO$_3$, with the wall location marked by the black triangle, with a zoomed section in inset showing oxygen and niobium positions. Scale bar is 2 nm. (b) Simultaneously collected ADF-STEM image of the region imaged in Fig. 1(a), with the wall location marked by the black triangle. The zoomed section in inset shows the niobium atoms. Scale bar is 2 nm. (c) Averaged mean unit cell from the experimental data sets with the niobium positions in green and the oxygen atoms in red. The unit cell is shown as the black rectangle. (d) The schematic of the unit cell with the experimentally measured long and short dimensions. The niobium and oxygen centers are shown as green and red crosses with the projected Ising and Néel displacement directions. (e) Atomic model of LiNbO$_3$ crystal structure viewed from the [1$\bar{1}$00] zone axis, with lithium atoms in purple, niobium atoms in green, and oxygen atoms in red. The average unit cell for polarization calculations is shown as a black dashed box with the arrows referring to the polarization direction.

As expected, the Ising displacement direction and magnitude do not change in the bulk domain, in contrast to the Ising displacements right across the domain wall [Fig. 3(c)]. Additionally we observe Néel displacements both in the bulk domain [Fig. 3(b)] and at the domain wall [Fig. 3(d)], with visual inspection confirming lower absolute magnitudes in the bulk domain. To understand the variability of the polar niobium-oxygen displacements at the domain wall with respect to the domain, we calculated the absolute magnitude of the Ising and Néel displacements in Fig. 3(e). These
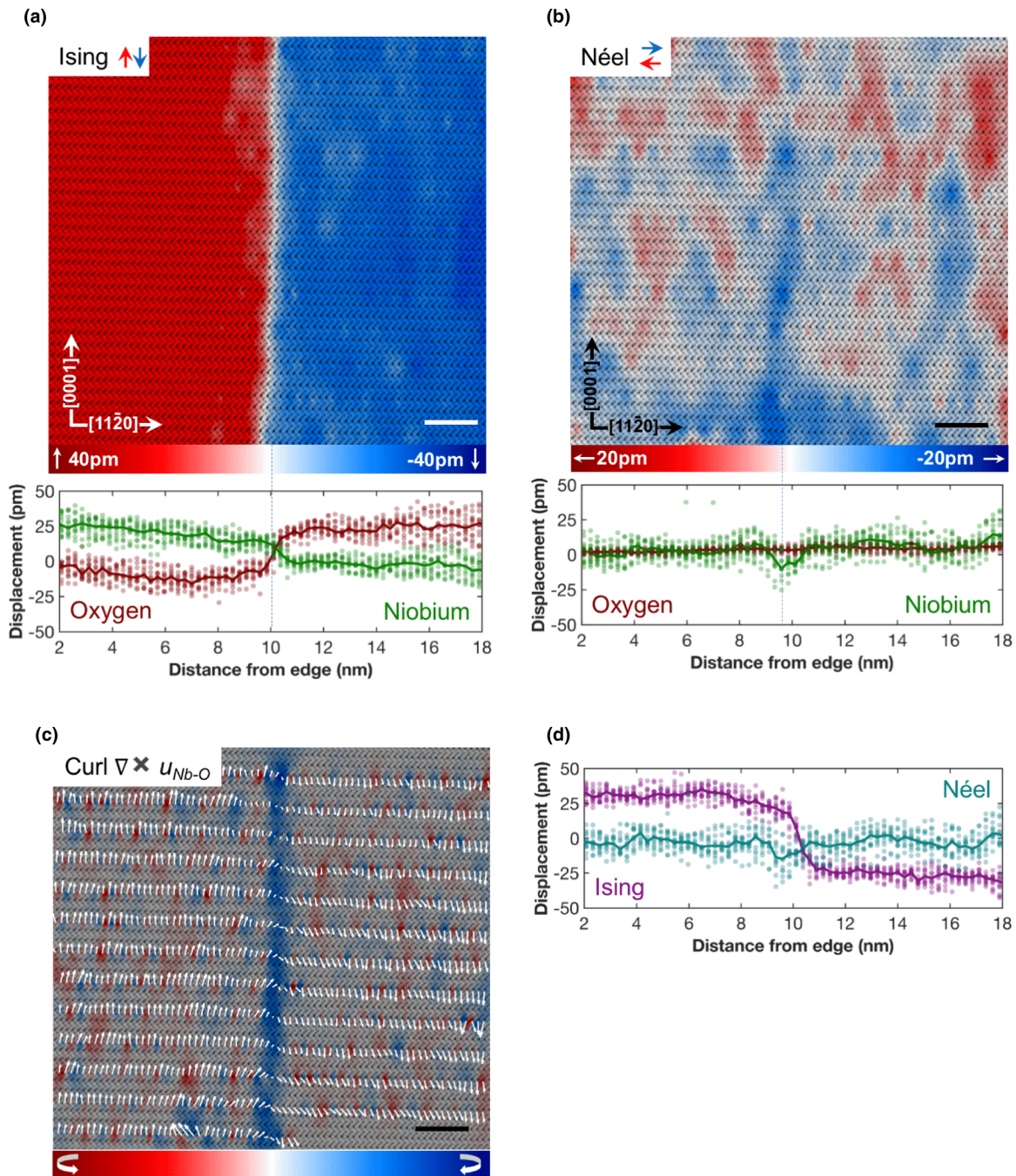
FIG. 2. Polar displacements measured with BF-STEM. (a) LiNbO$_3$ domain wall imaged from [$1\bar{1}00$] zone axis with the polar Ising niobium-oxygen displacements overlaid. Scale bar is 2 nm. The Ising niobium and oxygen along the $\langle 0001 \rangle$ direction in green and red, respectively, with the solid lines referring to the averages are plotted below. (b) Polar niobium-oxygen Néel displacements overlaid on the BF-STEM image. Scale bar is 2 nm. The Néel niobium and oxygen along the $\langle 11\bar{2}0 \rangle$ direction in green and red, respectively, with the solid lines referring to the averages are plotted below. (c) Curl of the niobium-oxygen displacement vector overlaid on the BF-STEM image, with the rotation vectors overlaid in white. (d) Niobium and oxygen relative Ising and Néel displacements.

measurements demonstrate the Néel displacements reaching values below 5 pm at distances over 100 nm away from the wall, but they do not completely die down. In contrast, the absolute magnitude of the Néel displacements increases in the proximity of the domain wall, along with a significantly higher spread in displacement magnitudes of both Ising and Néel displacements at the domain wall compared to the bulk domain. It should be noted that both the images were obtained

from the same TEM sample, and with the same exact imaging conditions. While microscope mechanical vibrations, sample preparation effects, and inhomogeneities in the chemical and atomic structure can locally induce random fluctuations, this long-range decrease in the magnitude of Néel displacements (at the domain wall as opposed to the bulk domain) are probably intrinsic to LiNbO$_3$ itself, originating from polar instabilities at the domain wall.
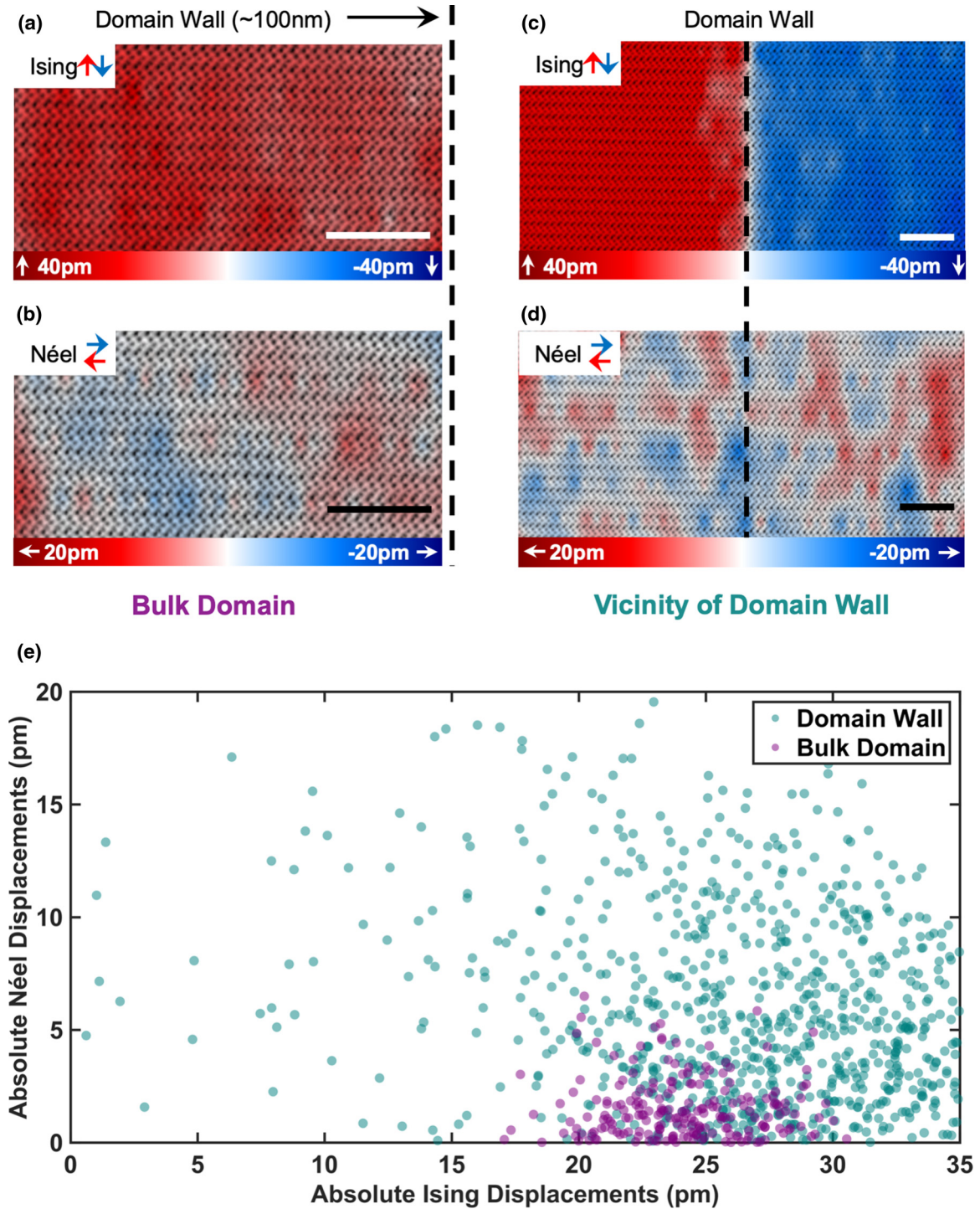
FIG. 3. Comparison of polar displacements at the bulk domain versus the domain wall. (a), (b) Ising and Néel Nb-O displacements in a region of the bulk domain, ≈100 nm away from the domain wall. Scale bar is 2 nm. (c), (d) Ising and Néel Nb-O displacements at the domain wall. Scale bar is 2 nm. (e) Comparison of the absolute magnitudes of the Ising and Néel Nb-O displacements in the two regions imaged in Figs. 3(a)–3(d) demonstrating the increased variability in displacement magnitudes at the domain wall compared to the bulk domain.

IV. FIRST-PRINCIPLES CALCULATIONS OF DISPLACEMENT ENERGETICS

To understand the origin of the observed polar instabilities, we performed density functional theory (DFT) calculations of phonons in the high-symmetry phase of $LiNbO_3$. In agreement with previous calculations we observed three unstable modes at the Γ point: A_{2u} and E_u polar modes with polarization parallel and perpendicular to the [0001] direction, respectively, and the A_{2g} Raman mode (see Fig. 12 and Table II) [26]. The polar A_{2u} mode has a significant overlap with the vector representing the atomic displacements during the phase transition and therefore describes the displacement pattern responsible for the Ising macroscopic
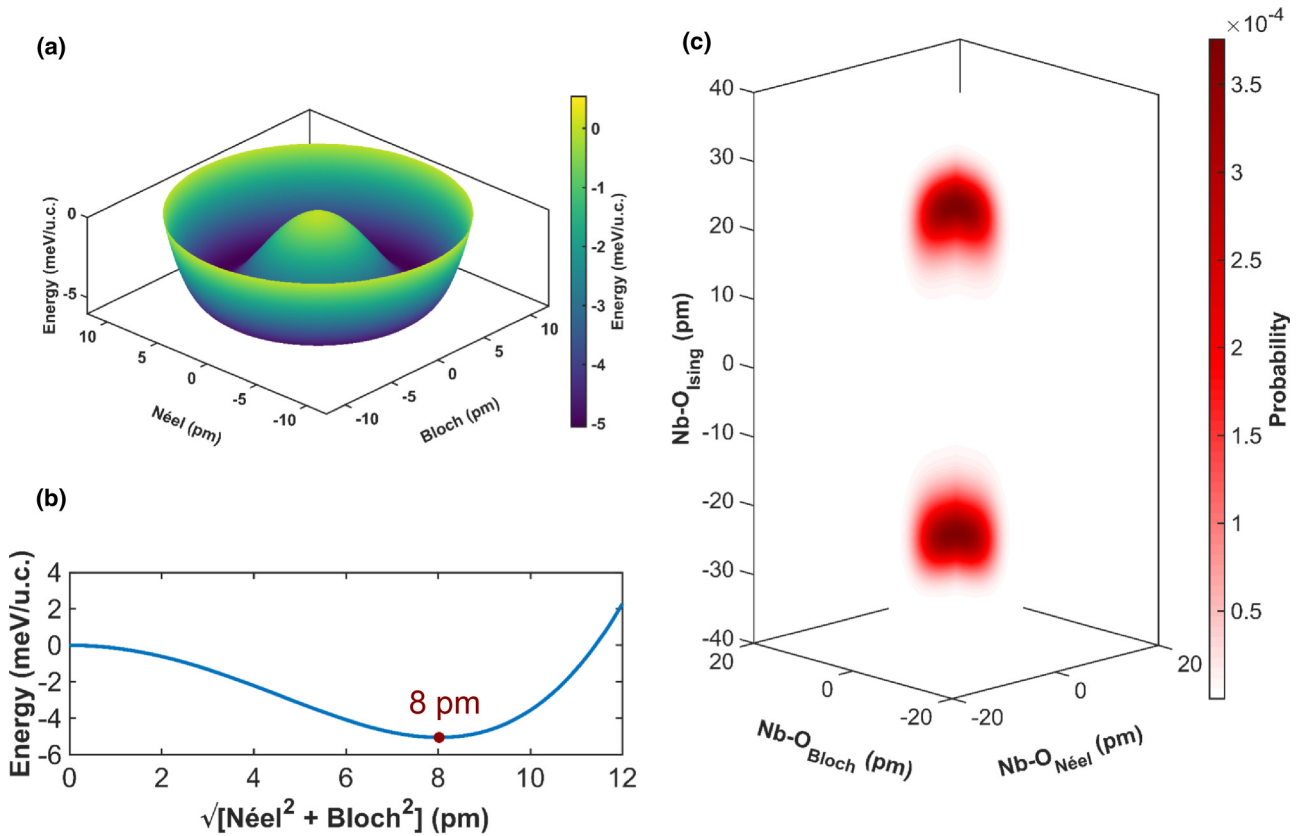
FIG. 4. First-principles calculations of displacement configurations. (a) Goldstone sombrero potential of the relative energy of LiNbO$_3$ with polar Néel and Bloch displacements associated with the E_u unstable mode. (b) Energy change as a function of the combined Néel and Bloch displacement magnitude, with energy minima at 8 pm. (c) Probability of displacements as a function of the Ising, Néel, and Bloch displacements from mean field effective Hamiltonian.

polarization of the ground-state ferroelectric phase of LiNbO$_3$.

Moreover, we observe that the polar displacements along the Néel/Bloch direction (associated with the doubly degenerate E_u mode) are unstable and the system can thus lower its energy with polar displacements perpendicular to the [0001] Ising direction. This can explain our experimental results, i.e., the presence of Néel and Bloch polarization directions at the domain wall where the Ising polarization amplitude is strongly reduced along the Ising direction. Aside from that, within a bulk ferroelectric domain, the E_u mode instability is suppressed by the A_{2u} mode condensation and the associated strain relaxation, however, the energy landscape is still sufficiently shallow to allow deviations of local dipole directions from the Ising $\langle 0001 \rangle$ axis. Thus, while the A_{2u} mode is the dominant mode driving ferroelectricity, the instability from the E_u modes makes it energetically favorable for the non-Ising fluctuations to arise from the ideal LiNbO$_3$ polar configuration, thus increasing disorder in the system.

The resultant energy landscape related to the displacements of atoms strictly perpendicular to the $\langle 0001 \rangle$ Ising axis (E_u mode) complies with SU(1) unitary group rotation symmetry resulting in the famous Goldstone sombrero potential shape with zero Ising component [Fig. 4(a)]. The suppression of the Ising displacements in the $\langle 0001 \rangle$ direction thus leads to a spontaneous symmetry breakdown giving rise to the perpendicular Néel and Bloch components, with the radial

magnitude of the perpendicular components reaching an energy minima at 8-pm displacement [Fig. 4(b)]. We also note that the experimentally observed Néel magnitudes of approximately 10 pm at the domain wall [Fig. 2(d)] are close to the theoretically predicted displacement magnitude at the energy minima. Note, however, that these experiments cannot quantify the predicted Bloch displacements because transmission electron microscopy probes a two-dimensional projection of columns of atoms, and Bloch displacements would be parallel to the atomic columns. Thus, it was not possible to determine whether the magnitude of the non-Ising polar components stayed constant (massless Goldstone modes) or varied across the domain boundary (massive Higgs modes) [27,28]. These calculations demonstrate that even in a monodomain region, the shallow E_u mode permits fluctuations in the non-Ising polar components. This is shown in Fig. 4(c) where rather than the displacements being clustered at the canonical Ising value, there is a spread in displacement magnitudes in both the Néel and the Bloch directions. Thus, our theoretical calculations demonstrate that polar disorder is intrinsic to LiNbO$_3$ and is not just confined to the domain wall proximity.

V. PROBABILITY DISTRIBUTION OF POLAR DISPLACEMENTS

The standard accepted method for quantifying disorder is entropy. This can be succinctly expressed through the famous
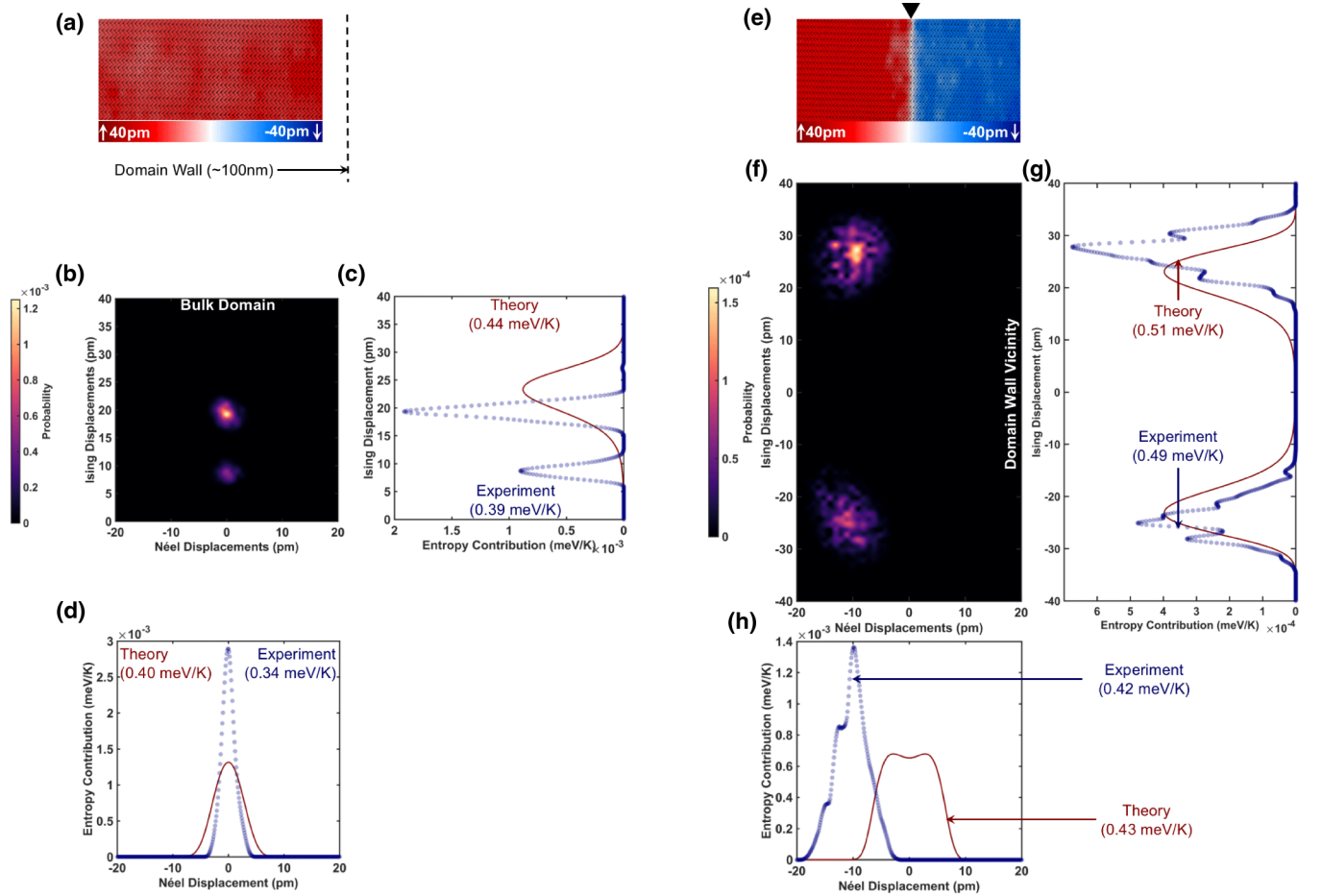
FIG. 5. Measured deconvolved probability and polar entropy in the bulk domain and domain wall proximity in LiNbO₃. (a) Representative STEM image of a bulk domain region approximately 100 nm to the left of the domain wall from where the probability distribution and entropy was measured with the Ising displacements overlaid demonstrating a monodomain region. Scale bar is 2 nm. (b) Richardson-Lucy deconvolved probability distribution of Ising and Néel displacement magnitudes in the bulk domain. (c), (d) Theoretically calculated (brown) and experimentally measured (blue) entropy contribution as a function of Ising and Néel displacement orientations in the bulk domain, with the summed contribution in the inset. (e) Representative STEM image of a region in the proximity of the domain wall with Ising displacements overlaid, with the black triangle marker at the top showing the domain wall location. Scale bar is 2 nm. (f) Richardson-Lucy deconvolved probability distribution of Ising and Néel displacement magnitudes in the proximity of the domain wall. (g), (h) Theoretically calculated (brown) and experimentally measured (blue) entropy contribution as a function of Ising and Néel displacement orientations in the proximity of the domain wall, with the summed contribution in the inset. The entropy deconvolution and calculation process is detailed in Appendix B.

Gibbs-Boltzmann's formulation [29]

$$S = -\sum_{N} k_B \rho \log(\rho), \tag{1}$$

where S is entropy, N is the number of states, k_B is the Boltzmann's constant, and ρ is the probability of a state. Thus, a single-state system has zero entropy, while entropy increases with increasing disorder, or increasing number of states. In this work, we measure polar entropy through the quantification of the probabilities of the observed polar displacements (ρ), where each possible displacement configuration is a single state. It can thus be deduced also that a monodomain system with a constant value of polar displacement has zero polar entropy.

Experimental quantification of the probabilities (ρ) of polar displacements along the Ising and Néel displacement orientations in the bulk domain [representative image shown

in Fig. 5(a)] is shown in Fig. 5(b). The measured displacements do not correspond to one single Ising value and are associated with a spread in Ising and Néel magnitudes with the most probable displacement configuration being 20 pm of Ising displacements and below 5 pm of Néel displacements. The Ising displacements demonstrate a bimodal behavior originating from the fluctuations in the ⟨0001⟩ intensities that were observed experimentally in the bulk domain. The origin of these fluctuations may be a consequence of local disorder, nonstoichiometry, or vacancy agglomeration in local regions. Further research is required to explain the origin of this Ising bimodal behavior within the bulk domain. Additionally, fluctuations in the electron beam may overestimate the disorder present in the system.

To measure the effect of the electron beam on the measured entropy, a series of Gaussian probability distributions were deconvolved from the experimentally measured displacements,

and the resulting probability distributions that resulted in the lowest entropy value were chosen. Considering the deconvolution of the Gaussian probability distributions, we have calculated a standard deviation (σ) of 8.7 pm at the bulk domain and 11.7 pm at the domain wall for the microscope instability (detailed in Appendix B). It should be noted that this σ is similar in magnitude to error distributions reported in previous STEM measurements of oxide displacements [30]. The deconvolution procedure thus removes any global fluctuations in the data, which arise notably from microscope instabilities. However, surface damage is expected to create random displacements with no long-range order as is observed in the experimental analysis. In this experiment, the sample damage was minimized by choosing a low final milling energy of 500 V (see Appendix A).

The resulting probability distribution after the deconvolution process is used to calculate the polar entropy contribution as a function of the possible Ising and Néel states. Figure 5(c) demonstrates the theoretical and experimental contributions to entropy as a function of Ising displacement configurations, with the total Ising entropy being the sum of the contributions of the individual Ising displacements. Both first-principles calculations and experiments demonstrate that a nonzero polar entropy originating from a spread in displacement configurations to be present even in the bulk domain. This picture is repeated even when measuring the entropy arising as a consequence of a spread of Néel displacement probabilities, as shown in Fig. 5(d). The integrated entropy associated with the Néel component is measured as 0.31 meV/K from experiment, while theory predicts an intrinsic value of 0.4 meV/k. The integrated Ising entropy [calculated by integrating the curves in Fig. 5(c)] are 0.4 meV/K (experiment) and 0.44 meV/K (theory). Thus, both the measured and theoretically predicted Ising and Néel contributions to the polar entropy are within 10% of each other, indicating the intrinsic nature of these fluctuations.

This picture changes in the proximity of the domain wall [defined here as $\approx \pm 10$ nm across the wall, with the STEM image of the representative section shown in Fig. 5(e)], whose probability distribution is plotted in Fig. 5(f). As expected, we observe a bimodal distribution of the probable polar states in the proximity of the wall owing to two domains being imaged rather than one, with a significantly more diffuse probability distribution as compared to the probabilities measured in Fig. 5(b). Both the integrated experimental and the theoretically predicted entropy contributions shown in Figs. 5(g) and 5(h) increase in the proximity of the domain wall when compared to the bulk domain. The experimentally measured polar entropy in the proximity of the wall is approximately 28% higher than the bulk domain entropy far away from the wall. In fact, since electron microscopy measurements project a three-dimensional object into a two dimensions, our measurements underestimate the entropy due to the absence of Bloch displacements in the calculations. This can be understood by the fact that entropy necessarily refers to random displacements, thus even along the Ising and Néel directions we are measuring a column averaged displacement, not the disorder of individual unit cells. This explains to a certain extent why the experimental entropy measurements are lower than their theoretically predicted values.

VI. CONCLUSIONS

Our results presented here are experimental quantifications of configurational entropy of polar displacements from atomic resolution position metrology. Theoretically predicted and experimentally measured entropy reveals a classical single-crystal Ising ferroelectric, hiding considerable local intrinsic disorder that is present even in the bulk domain. This is despite LiNbO$_3$ having only a single symmetry-allowed net polarization direction, large coercive fields for domain reversal, and a high Curie temperature indicating its stability at room temperature [25,31–33]. We show that this disorder is intrinsic to ferroelectrics and can exist even in the absence of any extrinsic factors. While previous theoretical studies have demonstrated the effect of entropy in controlling polar behavior halide perovskites, here we demonstrate experimentally that entropy is considerably more prevalent [34]. Polar disorder is a highly sought after component for functional systems like piezoelectrics and electrocalorics, and our study reveals it to be present even in systems thought to be more uniform like LiNbO$_3$ [35–38]. The electron microscopy based metrology techniques developed here thus allow for similar studies to be performed in other systems, even beyond ferroelectrics, allowing the electron microscope to be used not only as an imaging system, but also for atomic resolution thermodynamic quantification.

APPENDIX A: ELECTRON MICROSCOPY OF LiNbO$_3$

For this study, we used commercially available periodically poled single-crystal congruent LiNbO$_3$ crystals with 6.7-μm domain repetition from Deltronic Industries. The electron transparent samples were prepared by focused ion beam (FIB)
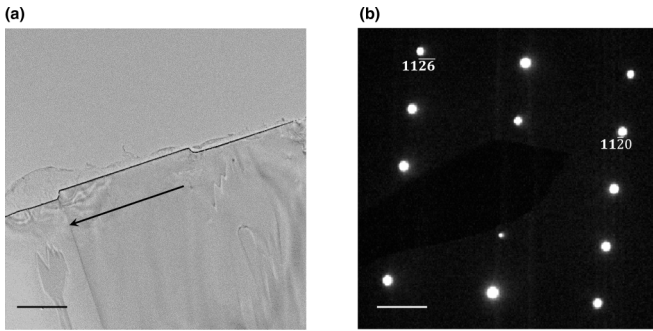
FIG. 6. Low-magnification TEM image and electron diffraction pattern. (a) Low-magnification CTEM with the domain wall (marked by the arrow) visible due to diffraction contrast at the wall. (b) Diffraction pattern from the image in (a) confirming the [1$\bar{1}$00] zone axis.

using a FEI Helios G2 system with a 30-keV gallium ion beam used for sample lift-out with the domain walls lying edge on, as seen from the low magnification HRTEM image in Fig. 6(a). The simultaneous diffraction pattern shown in Fig. 6(b) confirmed the sample was observed from the [1$\bar{1}$00] zone axis. Final polishing was performed with 0.5-kV ion beams until the sample became electron transparent at an acceleration of 2 kV to ensure that the sample was thin enough for imaging oxygen atoms [39]. FIB was chosen for its advantage in site-specific sample preparation. The extent of amorphous surface damage is proportional to the ion accelerating voltage, at low energies such as 2 kV, the amorphous layer thicknesses are approximately 0.5–2 nm thick [40,41]. A recent work has demonstrated that low-voltage ion milling at 0.4 kV completely eliminated amorphous surface layers [42]. In fact, FIB has been recently used for preparing battery electrolyte TEM samples too, with no apparent damage to the sample [43]. The prepared samples were found to have a sample thickness ranging between 20–25 nm, as estimated with EELS inelastic mean-free path measurements (Fig. 7) [22].

Following the preparation of electron transparent samples, we first imaged the LiNbO$_3$ foil with conventional TEM (CTEM) mode at a slight defocus to locate and identify the domain walls from their diffraction contrast. Following the identification of the domain walls, we subsequently used STEM imaging in a spherical aberration corrected FEI Titan^3 transmission electron microscope, corrected for up to

third-order spherical aberrations. Annular dark field scanning TEM (ADF-STEM) imaging was performed using Fischione detectors at a camera length of 145 mm with an inner collection semiangle of 32 mrad, and an outer collection semiangle of 188 mrad. Bright fieldsScanning TEM (BF-STEM) images were simultaneously collected with Gatan detectors with an outer collection semiangle of 15 mrad. Simultaneous BF-STEM and ADF-STEM imagings were performed with fast scan directions oriented at $-5°$ and $85°$ with respect to the $\langle 11\bar{2}0 \rangle$ crystallographic axis. The two image sets were combined and subsequently corrected post acquisition for scan drift using a previously developed procedure [44]. After acquiring the atomic resolution BF-STEM images, we used MATLAB scripts to refine the positions for subpixel precision displacement metrology. To perform the refinement, we started by locating the highest intensity spots as a first pass to estimate atom positions in ADF-STEM and inverted contrast BF-STEM images. We performed subsequent refinement by fitting a multipeak two-dimensional Gaussian to the observed atom intensity distribution to get the atom positions with a precision approaching ≈ 2 pm [30].

APPENDIX B: QUANTIFICATION OF POLAR ENTROPY

Entropy measurements are performed using STEM data acquired at both the domain wall and the bulk domain. Since the average pixel size for the experimental setup is approximately 10 pm, and the approximate image size is approximately 2000 × 2000 pixels, a representative image can visualize a 400-nm^2 area. Thus, images captured at the domain wall with the domain wall centered in the image field of view still have approximately 10 nm of the domain on either side. Entropy calculations are performed on one full image, and thus domain wall entropy measurements also include contributions from approximately 10 nm of the domain on either side of the boundary. On average, the BF-STEM images from our experimental conditions correspond to approximately 800 unit cells. The polar displacements at each of the individual locations were subsequently sorted into 0.1-pm bins, from -50 pm (minimum) to 50 pm (maximum) of displacement magnitude, both for Ising and Néel displacements with a total of 1001 × 1001 possible displacement configurations. Thus, if a certain unit cell corresponds to an Ising displacement of 25.386 pm, and a Néel displacement of -12.456 pm, it will
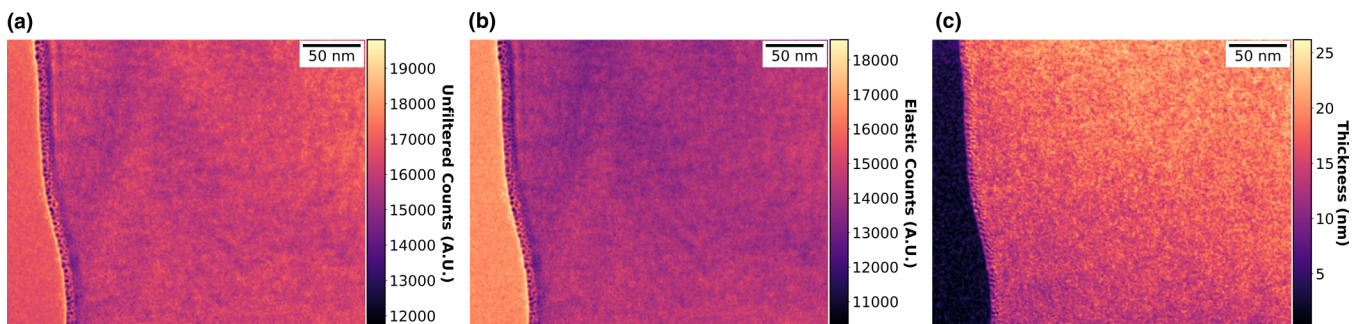
FIG. 7. Quantification of sample thickness through EELS. (a) Low mag unfiltered (zero-loss and core-loss) EFTEM image. (b) Simultaneously acquired elastic scattering (zero-loss) EFTEM image. (c) Quantified thickness from the log of the ratio of the total inelastic and elastic (a) and elastic (b) scattering contributions, demonstrating an average thickness of approximately 20–25 nm throughout the sample [22].
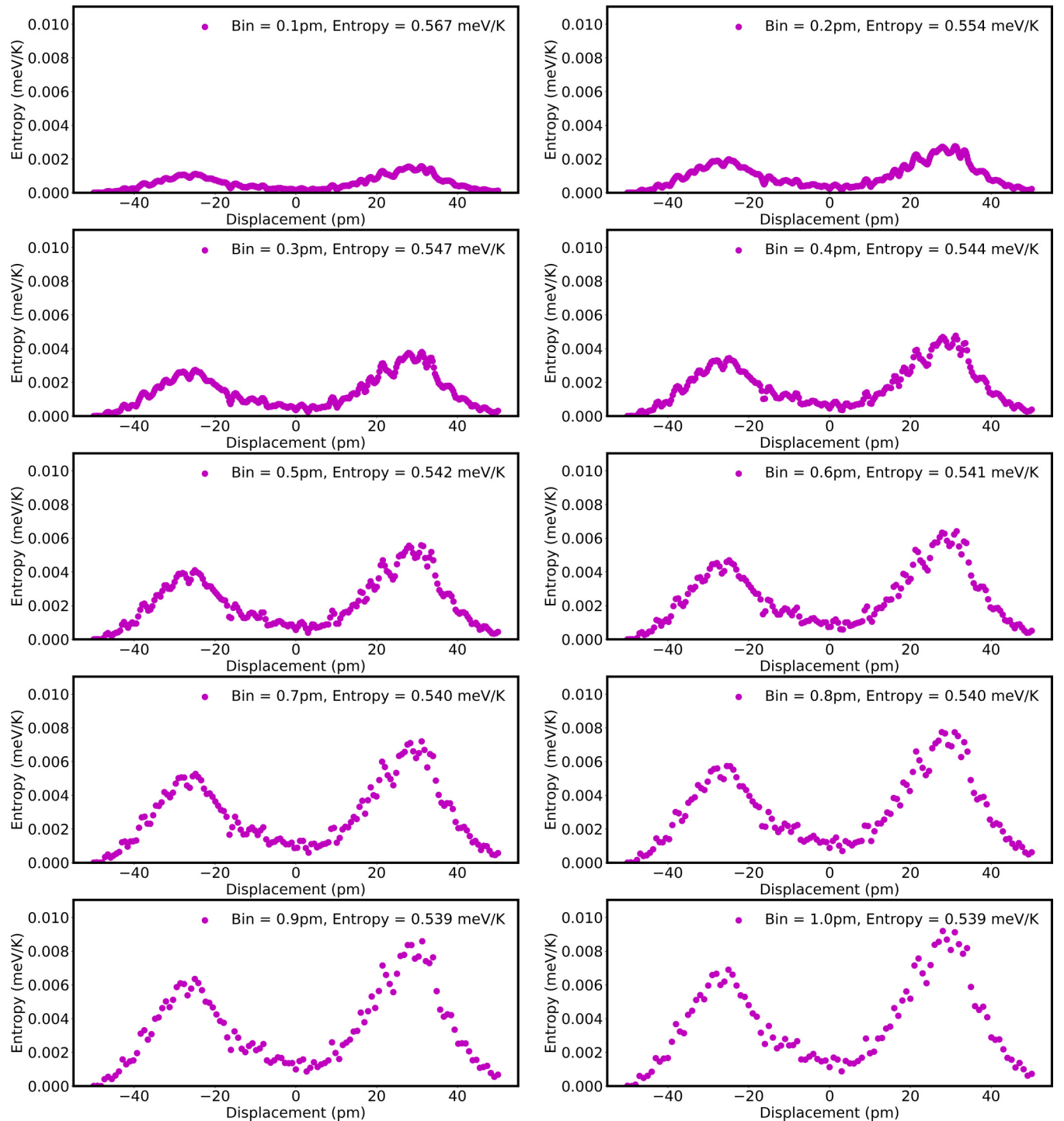
FIG. 8. Measured polar entropy for Ising displacements at the domain wall as a function of the displacement bin size, ranging from 0.1-pm bin size to 1-pm bin size.

be assigned to the bin corresponding to the displacements of 25.3 to 25.4 Ising displacements, and -12.5 to -12.4 pm of Néel displacements with one unit cell corresponding to one displacement observation. Following assignment of all the observed displacements for one full image into their respective bins, the total number of observations for each bin is divided by the total observations made for the entire image. This is the probability (ρ) of observing a displacement corresponding to that bin position.

To quantify the effect of displacement bin size in estimating the entropy, we redid the calculations on one of the data sets: Ising entropy calculations at the domain wall with varying bin sizes from 0.1 to 1 pm as shown in Fig. 8. Choosing a 1-pm bin size rather than a 0.1-pm bin size results in a reduction of the entropy from 0.567 to 0.539 meV/K, which is $\approx$ a 5% reduction in the measured entropy. Thus, we can see that the entropy we measure is almost independent of the bin size. This can be explained by the fact that while the
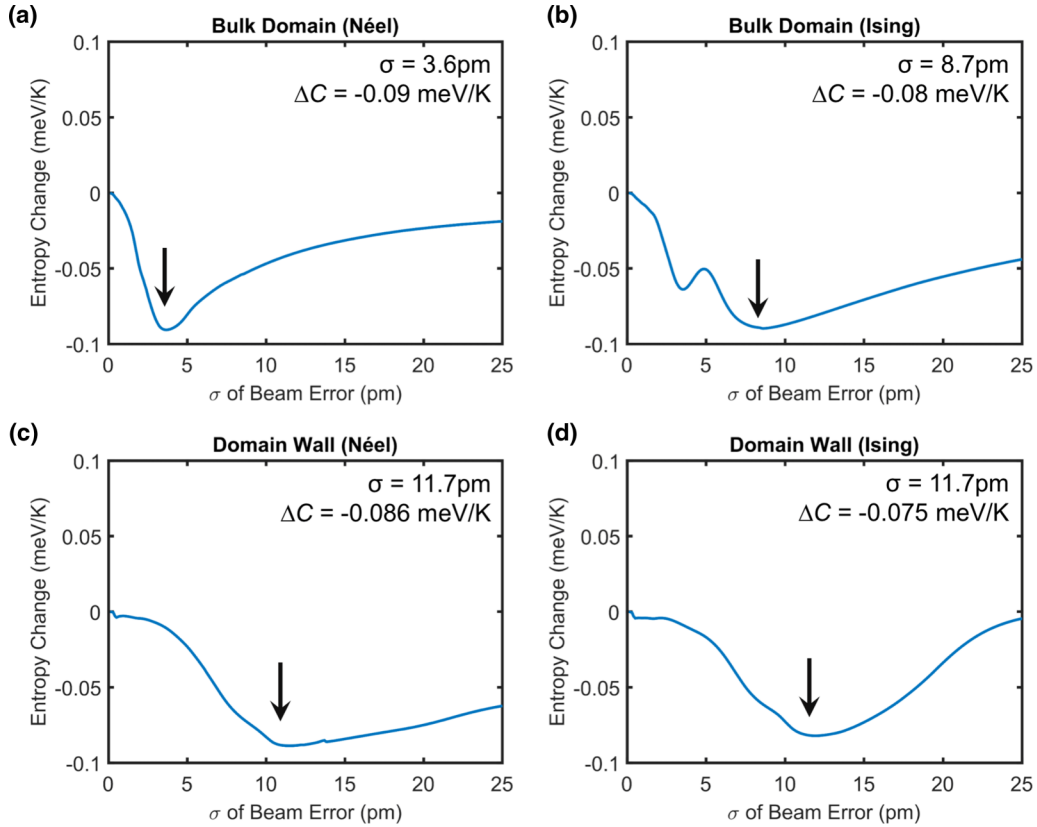
FIG. 9. Plotting the decrease in entropy as a function of the beam effects. (a) Change in measured entropy as a function of the measured σ of the Gaussian of the beam probability function for Néel displacements inside the bulk domain ($\approx$100 nm away from the domain wall). The minima is at 3.6 pm. (b) Change in measured entropy as a function of the measured σ of the Gaussian of the beam probability function for Ising displacements inside the bulk domain ($\approx$100 nm away from the domain wall). There are two minima, at 3.6 and 8.7 pm. (c) Change in measured entropy as a function of the measured σ of the Gaussian of the beam probability function for Néel displacements in the proximity of the domain wall. The minima are at 11.7 pm. (d) Change in measured entropy as a function of the measured σ of the Gaussian of the beam probability function for Ising displacements in the proximity of the domain wall. The minima are at 11.7 pm.

entropy contribution term $[k_B \rho \log(\rho)]$ in Eq. (1) from a single displacement bin increases with increasing the bin size due to an increase of the displacement probability ρ, however, this also leads to a reduction in the total number of displacement bins (N), and thus the entropy which is integrated over all the possible displacement values remains fairly constant.

A shortcoming of this technique is, however, rooted in the fact that the measured entropy is a function of the total observed vibrational probability, which is a combination of the *intrinsic* disorder of the system itself, instabilities in the electron microscope, and induced entropy originating from the interaction between the crystal and the electron beam. While it is the intrinsic material entropy that we ideally want to measure, because of the latter two effects our measured entropy overestimates the entropy in the system. Since these measurements were performed using a single crystal of LiNbO$_3$, where there is a remnant intrinsic entropy even in the bulk domain, there is no reference lattice to measure the microscope instabilities.

In fact, even a reference lattice measurement may underestimate entropy, for example, SrTiO$_3$, an ubiquitous oxide substrate is an incipient ferroelectric, with thin freestanding SrTiO$_3$ being a ferroelectric [45]. Polar fluctuations may not be limited to LiNbO$_3$ only, and it is highly conceivable that an entropy measurement of the substrate will also measure the intrinsic polar fluctuations of the substrate and thus overestimate microscope vibrations.

To estimate the contribution from measurement we assume that the instabilities can be expressed as a two-dimensional Gaussian distribution with a σ_x and a σ_y. The same assumption was also made for electron beam induced atom vibrations, and this is justified since the Debye-Waller parameters for both niobium and oxygen ($u_{\mathrm{Nb}} = 0.3924$ and $u_{\mathrm{O}} = 0.5$ [46]) can be approximated as scalars rather than tensors [46]. Since the convolution of a Gaussian kernel with another colocated Gaussian kernel is also a Gaussian, thus, the total nonintrinsic microscope instability contribution ($\rho_{x,y}$) can be reasonably approximated as a two-dimensional Gaussian function where x and y are the Cartesian displacement directions.

Thus, the Gaussian function can be written as

$$\rho_{x,y} = \frac{1}{\sqrt{2\pi}\sigma} e^{-\frac{1}{2}\left(\left(\frac{x-\mu_x}{\sigma_x}\right)^2 + \left(\frac{y-\mu_y}{\sigma_y}\right)^2\right)} \delta x\, \delta y. \quad (B1)$$

This is a probability distribution since

$$\int_{-\infty}^{\infty}\int_{-\infty}^{\infty} \rho_{x,y} = \int_{-\infty}^{\infty}\int_{-\infty}^{\infty} \frac{1}{\sqrt{2\pi}\sigma} e^{-\frac{1}{2}\left(\left(\frac{x}{\sigma_x}\right)^2 + \left(\frac{y}{\sigma_y}\right)^2\right)} \delta x\, \delta y \quad (B2)$$

$$= 1. \quad (B3)$$
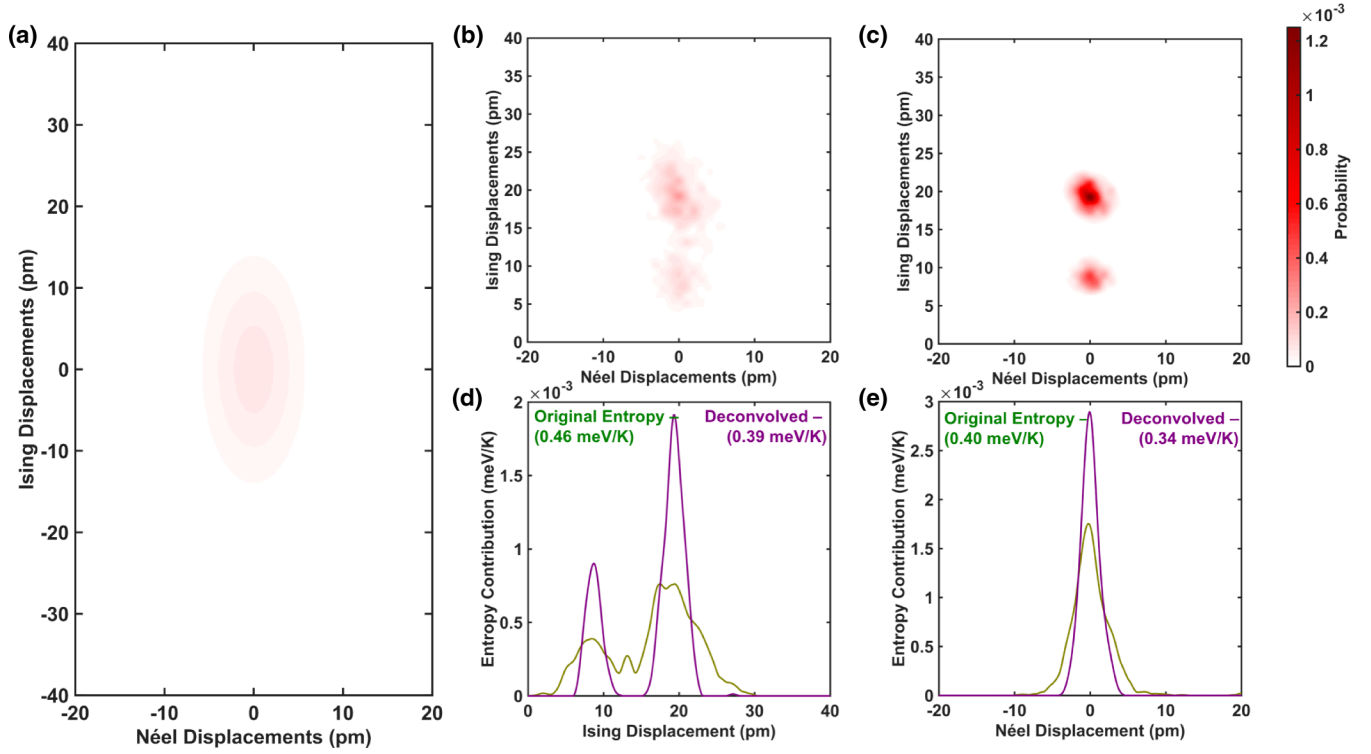
FIG. 10. Deconvoluting the microscope effects in the bulk domain. (a) Gaussian estimation of the microscope instabilities with $\sigma_{\text{Neel}} = 3.6$ pm and $\sigma_{\text{Ising}} = 8.7$ pm. (b) Experimentally calculated probability distribution of polar displacements in the bulk domain. (c) Richardson-Lucy deconvolved probability distribution of polar displacements in the bulk domain. (d) Comparison of original and deconvolved entropy measurements as a function of Ising displacements, demonstrating an $\approx 13\%$ reduction in entropy. (e) Comparison of original and deconvolved entropy measurements as a function of Néel displacements, demonstrating an $\approx 23\%$ reduction in entropy.

Since this is the microscope instability probability, the Gaussian is centered at $(\mu_x, \mu_y) = 0$, then Eq. (B1) can be expressed as

$$\rho_{x,y} = \frac{1}{\sqrt{2\pi}\sigma} e^{-\frac{1}{2}\left(\left(\frac{x}{\sigma_x}\right)^2 + \left(\frac{y}{\sigma_y}\right)^2\right)} \delta x \, \delta y. \qquad \text{(B4)}$$

. Using the Boltzmann definition of entropy, and inputing Eq. (B4) in Eq. (1)

$$\Delta S_e = k_B \left[\log\left(\sqrt{2\pi}\sigma_x + \sigma_y\right) + \tfrac{1}{2} \right], \qquad \text{(B5)}$$

where ΔS_e refers to the microscope contribution to measured entropy.

Thus, as Eq. (B5) demonstrates, the total entropy increases monotonically with σ_x and σ_y. To obtain the intrinsic probability, a deconvolution of the measured probability distribution function with a Gaussian probability distribution function (PDF) is thus required. It can be easily deduced that the microscope contribution to the entropy is mathematically analogous to a blurring function commonly encountered in optics. Thus, the experimentally measured probability is the material probability convolved by a point spread function (PSF) of the instrumental vibrations, with the PSF assumed to be Gaussian in this case. To deconvolve the underlying entropy, we can thus use the Richardson-Lucy deconvolution to iteratively obtain the unblurred PDF [47,48]. Mathematically, thus if ρ is the microscope instability probability distribution, and τ is the intrinsic fluctuation in polar displacements, it is

the following entropy we are after:

$$\Delta S_i = \int k_B \tau \log \tau. \qquad \text{(B6)}$$

Since, the measured probability distribution ϕ is a convolution, it can be written as

$$\phi = \theta \circ \rho \qquad \text{(B7)}$$
$$= \mathcal{F}(\mathcal{F}^{-1}(\tau) \times \mathcal{F}^{-1}(\rho)). \qquad \text{(B8)}$$

Thus, for a certain value of σ_x and σ_y, the deconvolved probability as a function of σ_x and σ_y can be expressed as

$$\tau_{\sigma_x, \sigma_y} = \mathcal{F}\left(\frac{\mathcal{F}^{-1}(\phi) \times \left(\mathcal{F}^{-1}\left(\rho_{\sigma_x, \sigma_y}\right)\right)^*}{\left|\mathcal{F}^{-1}\left(\rho_{\sigma_x, \sigma_y}\right)\right|^2}\right), \qquad \text{(B9)}$$

where $\mathcal{C}^*$ is the complex conjugate of a function $\mathcal{C}$.

Thus, the decrease in entropy ΔC as a result of the deconvolution

$$\Delta C_{\sigma_x, \sigma_y} = -k_B \left(\int \phi \log \phi - \int \tau_{\sigma_x, \sigma_y} \log \tau_{\sigma_x, \sigma_y} \right). \qquad \text{(B10)}$$

Since we do not possess a reference lattice from which a point spread function could be deduced, we measured $\Delta C_{\sigma_x, \sigma_y}$ for both Ising and Néel displacements in the bulk domain and at the domain wall. For Néel displacements in the bulk domain, the $\Delta C_{\sigma_x, \sigma_y}$ reaches a minima with a $\sigma_x = 3.6$ pm as demonstrated in Fig. 9(a). Qualitatively, this means that the PDF corresponding to this particular displacement can be
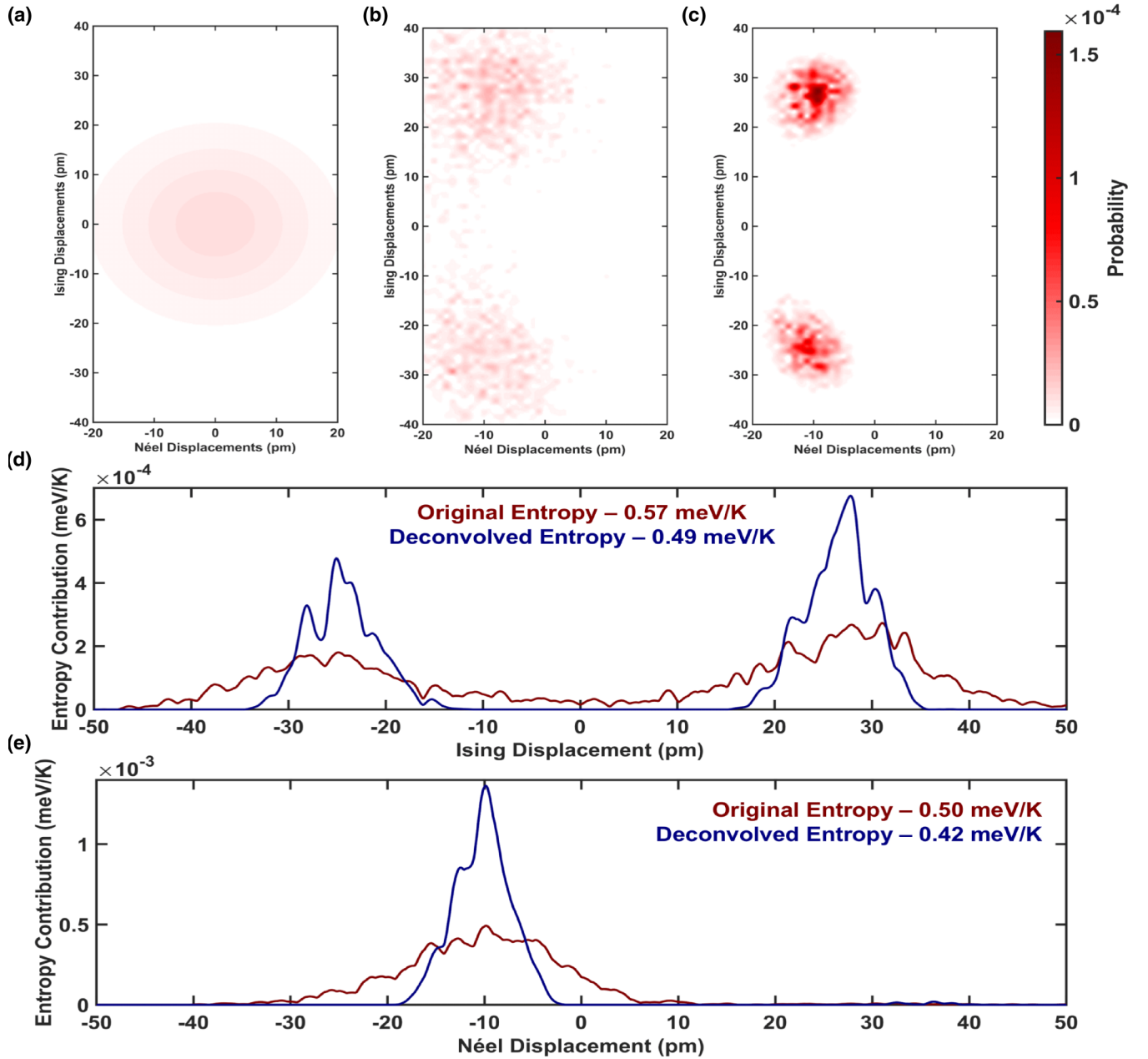
FIG. 11. Deconvoluting the microscope effects in the proximity of the domain wall. (a) Gaussian estimation of the microscope instabilities with $\sigma_{\text{Ising}} = \sigma_{\text{Neel}} = 11.7$ pm. (b) Experimentally calculated probability distribution of polar displacements in the proximity of the domain wall. (c) Richardson-Lucy deconvolved probability distribution of polar displacements in the proximity of the domain wall. (d) Comparison of original and deconvolved entropy measurements as a function of Ising displacements, demonstrating an ≈14% reduction in entropy. (e) Comparison of original and deconvolved entropy measurements as a function of Néel displacements, demonstrating an ≈16% reduction in entropy.

most closely be approximated a Gaussian of $\sigma_x = 3.6$ pm. Compared to the Néel displacements, when we plot $\Delta C_{\sigma_x, \sigma_y}$ for Ising displacements in the bulk domain in Fig. 9(b), we encounter two minima, one identical to the minima in Fig. 9(a) at 3.6 pm, and the second minima at 8.7 pm. The origin of this behavior could be understood by looking at the probability distribution of Ising displacements in the bulk domain [Figs. 5(b) and 5(c)] which is bimodal. For the most conservative possible estimate, thus, all domain probabilities were calculated after deconvolving the measured

probability distribution with a Gaussian of $\sigma_x = 3.6$ pm and $\sigma_y = 8.7$ pm.

Extending the deconvolution to the proximity of the domain wall, we observe that the maximum decrease in entropy occurs for both Néel and Ising displacements when the measured probability distribution function is deconvolved with a Gaussian with $\sigma = 11.7$ pm. It is interesting to note that the σ_x and σ_y are larger in the proximity of the domain wall than in the bulk domain. However, since the experimental data for both regions were acquired back to back in the same

TABLE I. Calculated hexagonal coordinates of atoms of the primitive unit cell of paraelectric $LiNbO_3$. The lattice parameters are $a = 518$ pm and $c = 1364.6$ pm.

Atom	Position
Li1	$(0, 0, \frac{1}{2})$
Nb1	$(0, 0, 0)$
O1	$\left(\frac{-1}{3}, \frac{-1}{3} + x, \frac{7}{12}\right)$
O2	$\left(\frac{1}{3} - x, -x, \frac{7}{12}\right)$
O3	$\left(x, \frac{1}{3}, \frac{7}{12}\right)$

TABLE II. Eigenvectors in Cartesian coordinates of the identified unstable phonon modes of paraelectric $LiNbO_3$.

Atom	Polar phonon modes			
	A_{2g}	A_{2u}	E_u	E_u
Li1	$\begin{pmatrix} 0.000 \\ 0.000 \\ 0.407 \end{pmatrix}$	$\begin{pmatrix} 0.000 \\ 0.000 \\ 0.683 \end{pmatrix}$	$\begin{pmatrix} 0.000 \\ -0.069 \\ 0.000 \end{pmatrix}$	$\begin{pmatrix} 0.069 \\ 0.000 \\ 0.000 \end{pmatrix}$
Li2	$\begin{pmatrix} 0.000 \\ 0.000 \\ 0.407 \end{pmatrix}$	$\begin{pmatrix} 0.000 \\ 0.000 \\ -0.683 \end{pmatrix}$	$\begin{pmatrix} 0.000 \\ -0.069 \\ 0.000 \end{pmatrix}$	$\begin{pmatrix} 0.069 \\ 0.000 \\ 0.000 \end{pmatrix}$
Nb1	$\begin{pmatrix} 0.000 \\ 0.000 \\ 0.259 \end{pmatrix}$	$\begin{pmatrix} 0.000 \\ 0.000 \\ 0.000 \end{pmatrix}$	$\begin{pmatrix} -0.384 \\ 0.356 \\ 0.259 \end{pmatrix}$	$\begin{pmatrix} -0.356 \\ -0.384 \\ 0.000 \end{pmatrix}$
Nb2	$\begin{pmatrix} 0.000 \\ 0.000 \\ 0.259 \end{pmatrix}$	$\begin{pmatrix} 0.000 \\ 0.000 \\ 0.000 \end{pmatrix}$	$\begin{pmatrix} 0.384 \\ 0.356 \\ 0.000 \end{pmatrix}$	$\begin{pmatrix} -0.356 \\ 0.384 \\ 0.000 \end{pmatrix}$
O1	$\begin{pmatrix} 0.029 \\ 0.017 \\ -0.297 \end{pmatrix}$	$\begin{pmatrix} 0.055 \\ 0.032 \\ -0.085 \end{pmatrix}$	$\begin{pmatrix} 0.002 \\ -0.272 \\ 0.012 \end{pmatrix}$	$\begin{pmatrix} 0.269 \\ -0.002 \\ -0.021 \end{pmatrix}$
O2	$\begin{pmatrix} -0.029 \\ 0.017 \\ -0.297 \end{pmatrix}$	$\begin{pmatrix} -0.055 \\ -0.032 \\ 0.085 \end{pmatrix}$	$\begin{pmatrix} -0.002 \\ -0.272 \\ -0.012 \end{pmatrix}$	$\begin{pmatrix} 0.269 \\ 0.002 \\ -0.021 \end{pmatrix}$
O3	$\begin{pmatrix} 0.000 \\ -0.033 \\ -0.297 \end{pmatrix}$	$\begin{pmatrix} 0.000 \\ -0.064 \\ -0.085 \end{pmatrix}$	$\begin{pmatrix} 0.000 \\ -0.268 \\ -0.024 \end{pmatrix}$	$\begin{pmatrix} 0.274 \\ 0.000 \\ 0.000 \end{pmatrix}$
O4	$\begin{pmatrix} 0.000 \\ -0.033 \\ -0.297 \end{pmatrix}$	$\begin{pmatrix} 0.000 \\ 0.064 \\ 0.085 \end{pmatrix}$	$\begin{pmatrix} 0.000 \\ -0.268 \\ -0.024 \end{pmatrix}$	$\begin{pmatrix} 0.274 \\ 0.000 \\ 0.000 \end{pmatrix}$
O5	$\begin{pmatrix} -0.029 \\ 0.017 \\ -0.297 \end{pmatrix}$	$\begin{pmatrix} -0.055 \\ 0.032 \\ -0.085 \end{pmatrix}$	$\begin{pmatrix} -0.002 \\ -0.272 \\ 0.012 \end{pmatrix}$	$\begin{pmatrix} 0.269 \\ 0.002 \\ 0.021 \end{pmatrix}$
O6	$\begin{pmatrix} 0.029 \\ 0.017 \\ -0.297 \end{pmatrix}$	$\begin{pmatrix} -0.055 \\ -0.032 \\ 0.085 \end{pmatrix}$	$\begin{pmatrix} 0.002 \\ -0.272 \\ 0.012 \end{pmatrix}$	$\begin{pmatrix} 0.269 \\ -0.002 \\ -0.021 \end{pmatrix}$

experimental session, it is highly unlikely that the microscope is quantifiably less stable at the domain wall than at the domain. Rather, any Gaussian features in the probability distribution function are in fact being assigned to the point spread function, and thus this technique of measuring entropy is actually slightly conservative: the deconvolved entropy is in reality *underestimating* the intrinsic material entropy.

Visually, we can understand the effect of the deconvolution by observing the $\sigma_x = 3.6$ pm and $\sigma_y = 8.7$ pm Gaussian distribution in Fig. 10(a), the original measured probability distribution in Fig. 10(b), and the deconvolved probability in Fig. 10(c) in the bulk domain. The deconvolved probability is significantly sharper and less spread out. This is borne out by a reduction of the Ising contribution of the entropy from 0.46 to 0.40 meV/K, a reduction of $\approx 13\%$, as demonstrated in Fig. 10(d). The Néel contribution to the entropy, plotted in Fig. 10(e), also declines by $\approx 23\%$ from 0.40 to 0.31 meV/K.

Similarly, plotting the effects of the $\sigma_x, \sigma_y = 11.7$ pm Gaussian point spread function in the proximity of the domain wall, we find a marked sharpening of the deconvolved probability distribution function in Fig. 11(c) when compared to the experimentally measured probability distribution in Fig. 11(b). This sharpening leads to a reduction of the Ising contribution to the entropy, as plotted in Fig. 11(d) by 14% from 0.57 to 0.49 meV/K. The Néel contribution to the entropy, plotted in Fig. 11(e), declines by 16% as a result of the deconvolution from 0.50 to 0.42 meV/K. Thus, while the deconvolution decreases the total measured entropy across the board, even using the most aggressive Gaussian kernel does

not result in zero entropy, showing that this polar entropy is intrinsic to the material itself.

Thus, we observe around $\approx 25\%$ reduction in the measured entropy due to the deconvolution. The entropy of
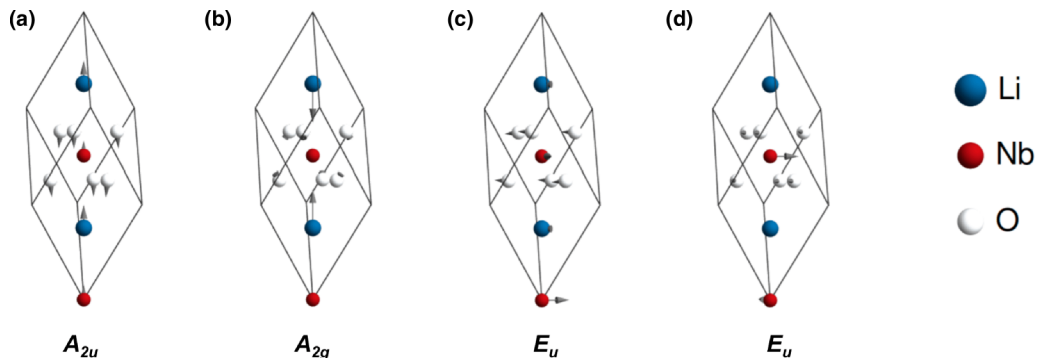
FIG. 12. Eigenvectors of the phonon modes. (a) The A_{2u} mode. (b) The A_{2g} mode. (c), (d) The two eigenvectors corresponding to the degenerate E_u mode aligned with x and y Cartesian axes, respectively.
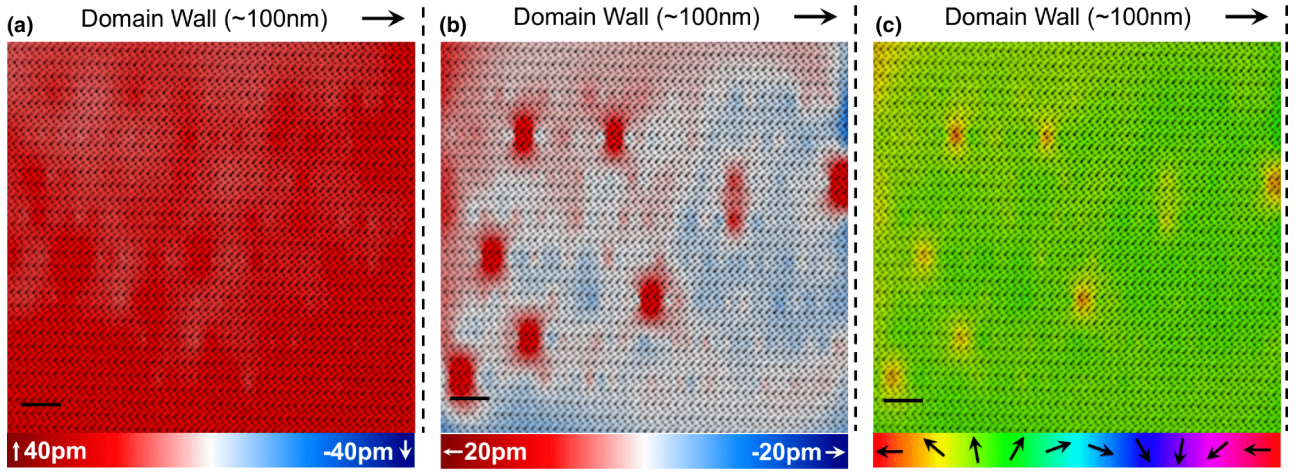
FIG. 13. Bulk domain HR-STEM image with the polarization and rotation map overlaid on top at a location ≈100 nm away from wall. (a) Ising displacement mapped out over the bulk domain. (b) Néel displacement map showing regions of no Néel displacements, and nanoregions of high Néel displacements. (c) Rotation color map. Scale bar in all images is 2 nm.

displacements (S) were subsequently calculated from the deconvolved probability distributions as per Eq. (1).

APPENDIX C: FIRST-PRINCIPLES CALCULATIONS

First-principles calculations were done using the density functional theory approximation as implemented in the ABINIT software package (v.8.4.3) [49–52]. We chose the LIBXC implementation of PBEsol GGA functional to describe the exchange-correlation energy contribution, and the valence electrons were tested through norm-conserving pseudopotentials obtained through the PseudoDojo project [53–57]. The plane-wave kinetic cutoff energy was taken to be equal to 50 Ha and the Brillouin zone was sampled using a $6 \times 6 \times 6$ Monkhorst-Pack mesh of special k points [58]. To determine the structure of the paraelectric $R\bar{3}c$ phase structure of LiNbO$_3$, we considered a primitive 10-atom unit cell and performed a relaxation of atomic positions followed by an energy optimization with respect to changes both in lattice vectors and the reduced atomic coordinates under an imposed constraint of the fixed $R\bar{3}c$ space-group symmetry,

with the primitive unit cell dimensions given in Table I. The high-accuracy structural relaxation was performed until the calculated force magnitudes were less than 10^{-8} ev per Å, and the absolute values of stress tensor components do not exceed 10^{-7} GPa. We performed density functional perturbation theory calculations (DFPT) so as to identify the unstable phonon modes (Table II). To construct the minimal effective Hamiltonian model, we have first computed the internal energy landscapes for all identified unstable modes. For this, we have performed DFT calculations of the total energy change upon gradually condensing the unstable modes into the structure. The resulting curves were fitted with the eighth-order polynomials as given by Eq. (C1):

$$E_M = \kappa_M x^2 + \alpha_M x^4 + \gamma_M x^6 + \delta_M x^8, \qquad (C1)$$

where x denotes the amplitude of the mode M. Similarly, performing calculations of energy changes induced by displacements involving not a single but two phonon modes allows to reconstruct the effective mode interactions that we take here to be of the form

$$E_{\text{int}}^{M_1 M_2} = g M_1 M_2 x^2 y^2, \qquad (C2)$$
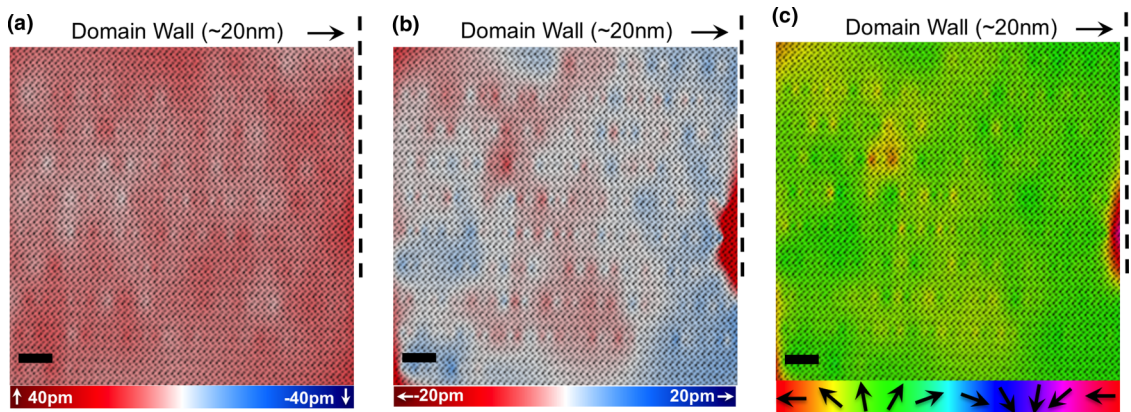
FIG. 14. Bulk domain ≈20 nm away from wall. (a) Ising displacement mapped out over the bulk domain, showing significantly lower displacements in comparison to other imaged regions. (b) Néel displacement map showing regions of lower Néel displacements. (c) Rotation color map. Scale bar in all images is 2 nm.
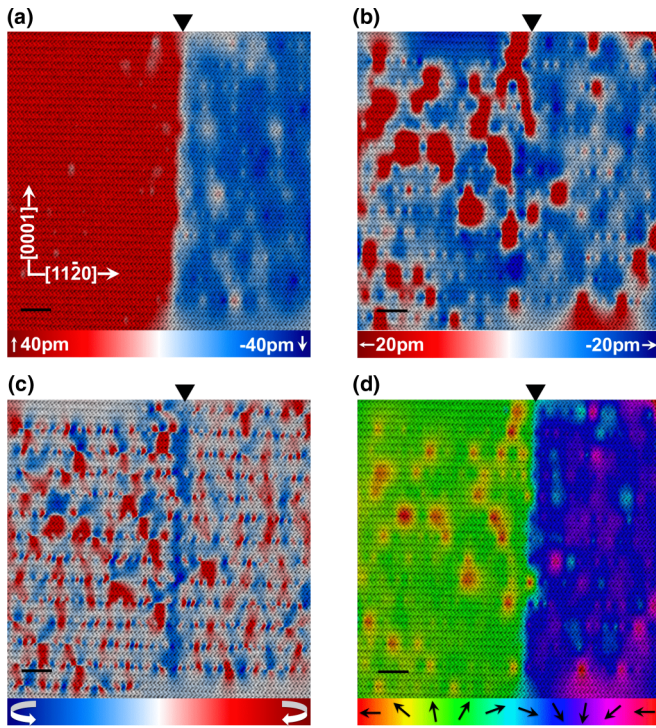
FIG. 15. Domain wall in region 2. (a) Ising displacements at region 2 of the domain wall with nonequivalent polarization on either side. (b) Néel displacements demonstrating the presence of strong alternating Néel components. (c) Curl of the polar niobium-oxygen displacement map with slight decrease at the domain wall. (d) Rotation map of the polar niobium-oxygen displacements. Scale bar in all images is 2 nm.

FIG. 16. Domain wall in region 3. (a) Ising displacements at region 3 of the domain wall with nonequivalent polarization on either side. (b) Néel displacements demonstrating the presence of consistent and uniform Néel components in contrast to region 2 (Fig. 15). (c) Curl of the polar niobium-oxygen displacement map with a small discernible change at the domain wall. (d) Rotation map of the polar niobium-oxygen displacements. Scale bar in all images is 2 nm.

where x and y denote the amplitudes of the M_1 and M_2 modes. The interaction of local modes with strain is taken into account by fitting the dependencies of elastic stresses on the mode amplitudes. Finally, the elastic energy produced by the deformations of the cell shape and volume is taken into account in the harmonic approximation. The elastic constants are computed from density functional perturbation theory. Note that in the case of the E_u mode, all the energy expansion coefficients are assumed to depend on the displacement direction in the (0001) plane, however, the calculations show that such in-plane anisotropy can be safely neglected. In the described model, the short- and long-range dipolar interactions between different modes are taken into account in the mean field approximation: these energetic contributions essentially lead to renormalization of the κ_M and $f_{M_1 M_2}$ coefficients. To determine the most important low-energy atomic displacement patterns, we further performed the density functional perturbation theory calculations so as to identify low-frequency phonon modes for the obtained ground state.

APPENDIX D: CALCULATION OF POLAR MODES

The calculated polar modes for the paraelectric LiNbO$_3$ unit cell (Table I) are shown in Table II. As could be observed, there are four polar modes, with the A_{2u} mode driving ferroelectricity, while it is the degenerate E_u modes that drive the non-Ising Néel and Bloch displacements. The

polar phonon mode displacements are visualized in Fig. 12, which plots the individual atom displacements corresponding to the polar modes.

APPENDIX E: DISPLACEMENTS IN THE BULK DOMAIN

Two different regions (Figs. 13 and 14) are shown as different regions of the bulk domain that were imaged. While all three are monodomain regions, it is instructive to note that the Ising displacement itself is not entirely constant even 100 nm into the domain, with the displacement demonstrating magnitude variations as seen in Fig. 13(a). These regions are additionally associated with regions of Néel displacements as can be observed in Fig. 13(b). These Néel displacements are ultimately visible in the rotation map [see Fig. 13(c)], demonstrating polar non-Ising components arising even in bulk domain regions approximately 100 nm away from the domain wall. This variation in polar components is ultimately reflected in increased entropy.

Figure 14 demonstrates a section of the bulk domain, approximately 20 nm away from the domain wall. As could be observed in this Appendix, the total Ising displacements are significantly smaller than expected, with a corresponding decrease in Néel displacements, demonstrating regions of decreased polarity embedded in the domain near the domain wall.
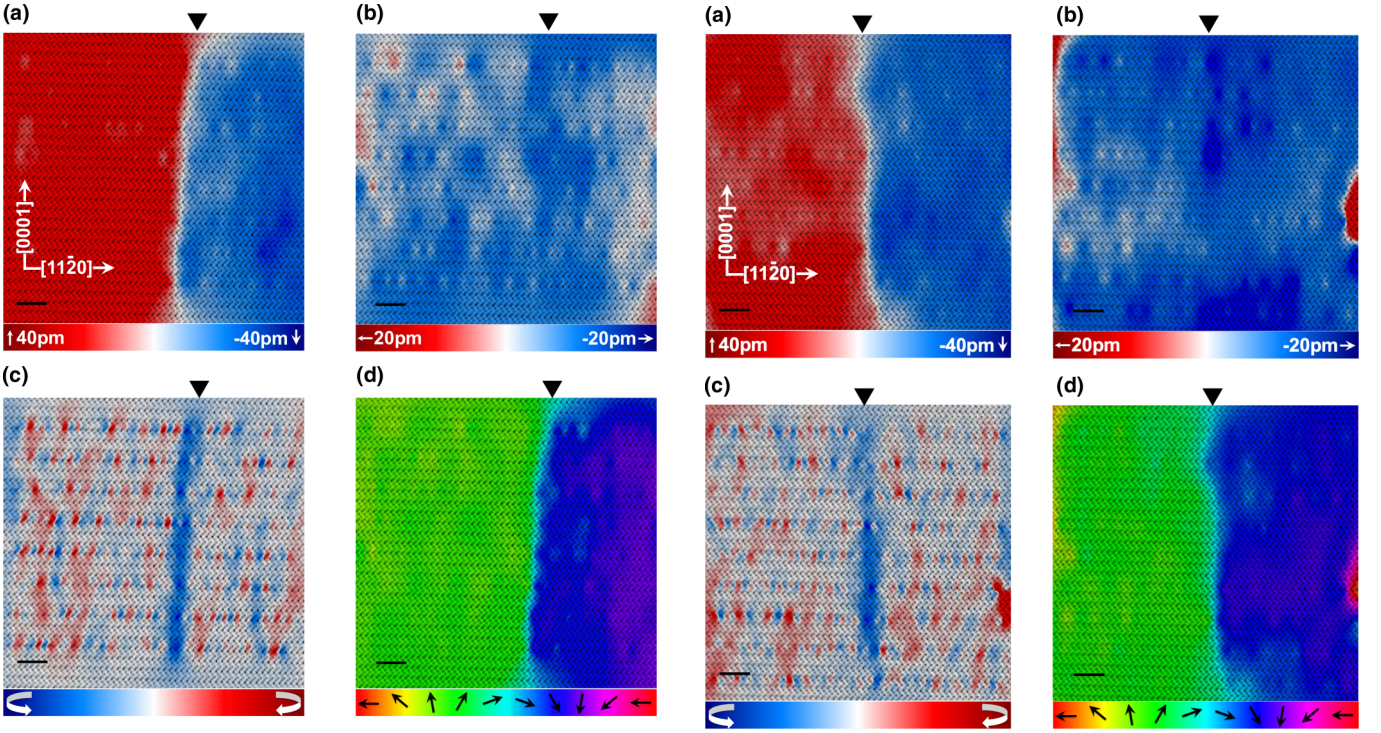
FIG. 17. Domain wall in region 4. (a) Ising displacements at region 4 of the domain wall with nonequivalent polarization on either side. (b) Néel displacements demonstrating the presence of Néel regions, not limited to only the domain wall. (c) Curl of the polar niobium-oxygen displacement map with a significant change only at the domain wall. (d) Rotation map of the polar niobium-oxygen displacements. Scale bar in all images is 2 nm.

FIG. 18. Domain wall in region 5. (a) Ising displacements at region 5 of the domain wall with a kink in the wall. (b) Quasiuniform Néel displacements in the proximity of the domain wall. (c) Curl of the polar niobium-oxygen displacement map. (d) Rotation map of the polar niobium-oxygen displacements, with the Ising kink being visible. Scale bar in all images is 2 nm.

APPENDIX F: DISPLACEMENTS IN THE THE PROXIMITY OF THE DOMAIN WALL

Four other domain wall regions (labeled as regions 2–5) in addition to the region imaged in the main text (Fig. 2) were imaged in the electron microscope, as demonstrated in Figs. 15–18. As could be observed from all the systems, the domain wall is consistently associated with significant Néel-type non-Ising distortions. One of the regions of the domain wall, Fig. 15, also demonstrates Néel distortions in both positive and negative directions, with leftward Néel distortions precipitating primarily at the domain wall. Also,

TABLE III. Calculated Born effective charges in LiNbO$_3$.

Atom	Cartesian direction	Born effective charge		
		1	2	3
Li	1	1.150619	$-1.860690 \times 10^{-16}$	5.756686×10^{-16}
	2	$-1.364568 \times 10^{-16}$	1.150619	4.525044×10^{-16}
	3	1.097943×10^{-16}	1.898622×10^{-13}	-1.103018
Nb	1	8.330707	-2.061953	2.317528×10^{-16}
	2	2.061953	8.330707	3.418674×10^{-16}
	3	-8.225340×10^{-1}	3.464213×10^{-12}	9.199131
O1	1	-3.848460	-1.191682	-2.153211
	2	-1.191682	-2.472424	-1.243157
	3	-2.048031	-1.182431	-3.434050
O2	1	-1.784406	$-3.133223 \times 10^{-17}$	2.586606×10^{-16}
	2	1.249054×10^{-17}	-4.536477	2.486314
	3	1.357373×10^{-16}	2.364863	-3.434050
O3	1	-3.848460	1.191682	2.153211
	2	1.191682	-2.472424	-1.243157
	3	2.048031	-1.182431	-3.434050
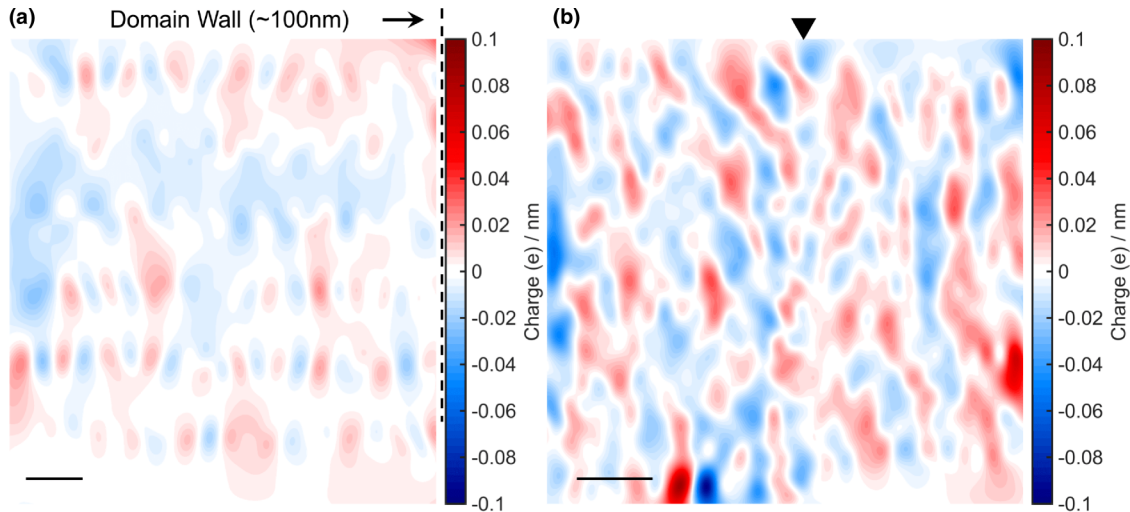
FIG. 19. Calculated charge accumulation. (a) Charge accumulation at a region of the bulk domain ($\approx$100 nm) away from the wall. The polarization maps are given in Figs. 13(a) and 13(b) for the Ising and Néel displacements, respectively. (b) Charge accumulation in the proximity of the domain wall (region 1), with the black triangle showing the domain wall location. The polarization maps are given in Figs. 2(a) and 2(b) for the Ising and Néel displacements, respectively. Scale bar in both images is 2 nm.

the thickness of the Ising component at the domain wall is not uniform at different regions of the domain wall, with Fig. 16 demonstrating significantly wider walls compared to the other regions imaged.

APPENDIX G: ESTIMATION OF CHARGE ACCUMULATION AND ELECTROSTATIC POTENTIAL ENERGY

We roughly estimated the charge accumulation from the polar distortions to get an estimate in the energy magnitudes of electrostatic potential energy and the thermodynamic free-energy decrease from the entropy.

Charge calculations were performed by first estimating the Born effective charge tensors theoretically, with the calculated Born effective charges presented in Table III. The calculated polar displacements from a representative bulk domain region (Fig. 13) and a a representative domain wall region (Fig. 2), respectively, are vector multiplied with the Born effective charge tensors (Table III) for the niobium and oxygen atoms only since we cannot image the lithium atoms. The divergence of this polarization is now the charge accumulation, which is presented in Fig. 19, with Fig. 19(a) showing the charge accumulation in the bulk domain region, and Fig. 19(b) demonstrating the charge accumulation in the domain wall proximity.

Thus, for each image, we have a total charge distribution. Assuming that each pixel corresponds to a charge value, then the total number of pixels (N) refers to the total possible charge values. The electrostatic potential energy is then
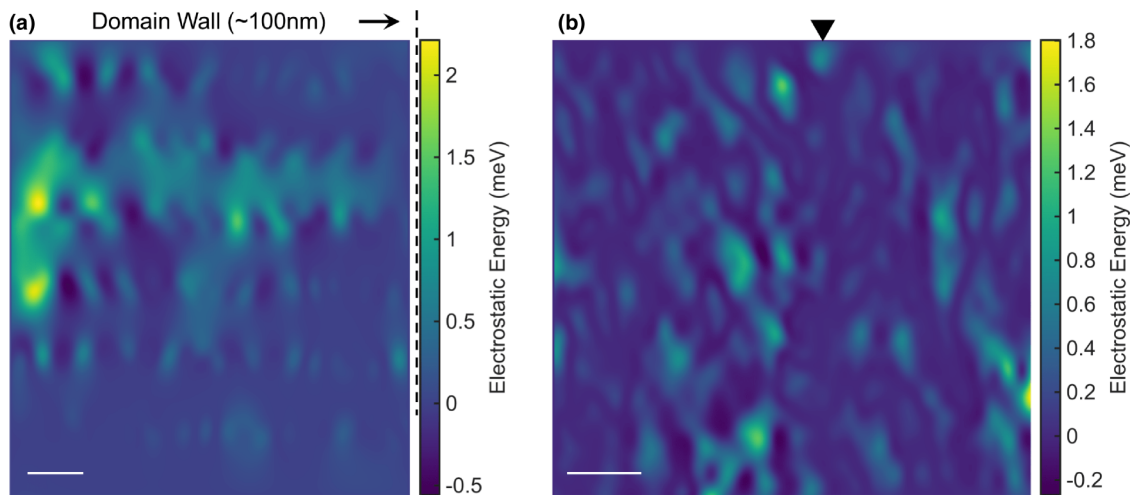
FIG. 20. Measured electrostatic potential energy. (a) Potential energy at a region of the bulk domain ($\approx$100 nm) away from the wall. The polarization maps are given in Figs. 13(a) and 13(b) for the Ising and Néel displacements, respectively. (b) Potential energy in the proximity of the domain wall (region 1), with the domain wall location shown by the black triangle. The polarization maps are given in Figs. 2(a) and 2(b) for the Ising and Néel displacements, respectively. Scale bar in both images is 2 nm. Potential energy was calculated with $\epsilon_r = 4.821$ [59].

TABLE IV. BF-STEM simulation conditions in MACTEMPASX.

Experimental conditions	Value
Crystal structure	$LiNbO_3$
Debye-Waller parameters	$u_{Li} = 0.67$ Å
	$u_{Nb} = 0.3924$ Å
	$u_O = 0.5$ Å [46]
Lattice parameters	$a = 5.172$ Å
	$b = 5.172$ Å
	$c = 13.867$ Å [60]
Space group	161 ($R3c$) [61]
Zone axis	$[1\bar{1}00]$
Accelerating voltage	200 kV
Inner collection angle	0 mrad
Outer collection angle	15 mrad
Cells	1×5
Frozen phonons	10
Slices per unit cell	5
Probe semiangle	28 mrad

calculated using Eq. (G1), obtained through an integration of Coulomb's law

$$U_E = \frac{1}{2} \Sigma_{x=1}^{N} q_x \Sigma_{y=1}^{N(y \neq x)} \left(\frac{1}{4\pi \epsilon_0 \epsilon_{LiNbO_3}} \times \frac{q_y}{r_{xy}} \right), \quad \text{(G1)}$$

where q_x refers to the charge at a certain pixel, and r_{xy} refers to the distance between distance between the xth and the yth pixel. The term $\frac{1}{2}$ prevents double counting the potential energy contribution between x and y, and y and x positions. The ϵ_{LiNbO_3} is 4.821 [59]. The calculated electrostatic potential energy for the two regions is shown in Fig. 20(a) for the domain and Fig. 20(b) for the domain wall.

The electrostatic potential energy in the bulk domain from our calculations of polarization comes out to be 0.37 meV in the bulk domain and 0.45 meV in the proximity of the domain wall. In contrast, the $-T\Delta S$ at 300 K is -213 meV at the bulk domain and -273 meV in the proximity of the wall. Thus, the magnitudes are significantly different, and electrostatics would not prevent polar fluctuations.

APPENDIX H: SIMULATION OF LiNbO$_3$ BF-STEM IMAGES

BF-STEM simulations of the $LiNbO_3$ crystal structure were performed using the MACTEMPASX commercial software to understand the effect of tilt on imaging and atom position metrology, with the simulation parameters being enumerated in Table IV, with the effect of increasing α tilt being shown in Fig. 21 [62]. As could be observed, the relative distance being the niobium-oxygen columns is sensitive to tilt, with the distance decreasing with increasing tilt. However, since the average niobium-oxygen polar Ising displacements match extraordinarily closely with the theoretical values in the domain wall figures presented in this work, tilt is not a contributing factor. Additionally, while increasing tilt would result in closer niobium-oxygen columns in the up domain, as shown in Fig. 21(c), it will also thus result in an increased distance in the down domain. However, the symmetric displacements observed (Figs. 2, 15–18) would indicate this is not in fact the case. Additionally, the effects of tilts should be global, with a constant increase or decrease in the displacement measured over the entire field of view. This is, however, not the case in any of the images presented, with the changes in the Ising or Néel displacements occurring over only a few unit cells.
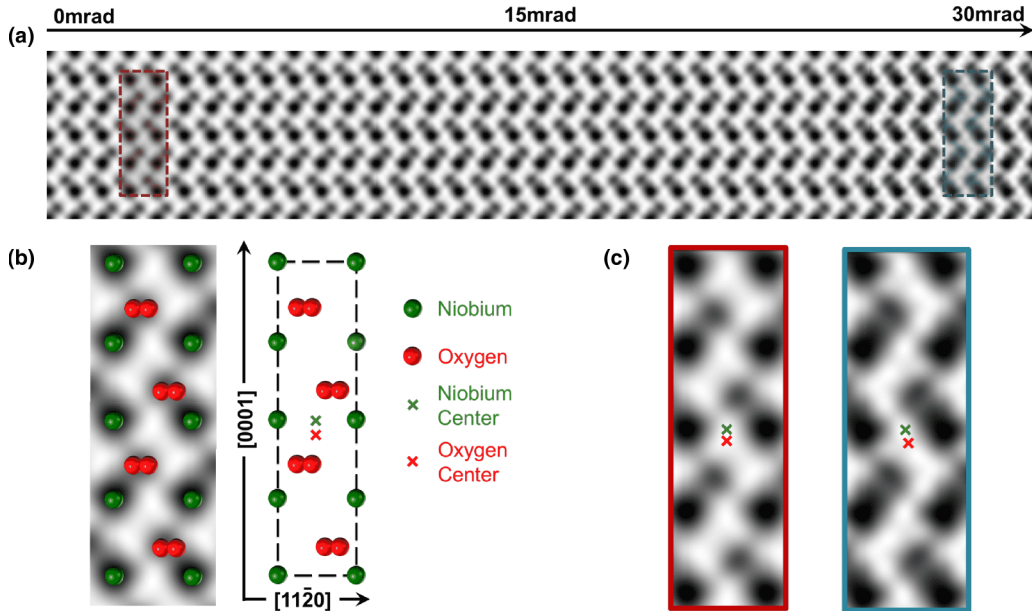
FIG. 21. Evolution of BF-STEM image as a function of α tilt. (a) Multislice simulations of BF-STEM image of $LiNbO_3$ using the conditions detailed in Table IV without aberrations as a function of α tilt from 0 mrad (no tilt) to 30 mrad of α tilt. (b) Zoomed-in section with the niobium atoms in green and the oxygen atoms in red overlaid on top. (c) Comparison of the tilt effects at 0 and 30 mrad showing how the relative displacement changes by 15 pm in the $[000\bar{1}]$ direction and by 25 pm in the $[11\bar{2}0]$ direction.

Considering that LiNbO$_3$ is a brittle oxide, and a 30-mrad tilt would result in enormous local stresses, it is safe to assume that it is local displacements rather than tilt which is being observed here.

[1] J. W. Gibbs, On the equilibrium of heterogeneous substances, Am. J. Sci. **96**, 441 (1878).

[2] J. J. Christensen, R. M. Izatt, L. D. Hansen, and J. A. Partridge, Entropy titration. a calorimetric method for the determination of ΔG, ΔH, and ΔS from a single thermometric titration[1a,b], J. Phys. Chem. **70**, 2003 (1966).

[3] *Physics of Ferroelectrics: A Modern Perspective*, edited by K. M. Rabe, C. H. Ahn, and J.-M. Triscone (Springer, Berlin, 2007).

[4] C. T. Nelson, B. Winchester, Y. Zhang, S.-J. Kim, A. Melville, C. Adamo, C. M. Folkman, S.-H. Baek, C.-B. Eom, D. G. Schlom *et al.*, Spontaneous vortex nanodomain arrays at ferroelectric heterointerfaces, Nano Lett. **11**, 828 (2011).

[5] K. Kimoto, T. Asaka, X. Yu, T. Nagai, Y. Matsui, and K. Ishizuka, Local crystal structure analysis with several picometer precision using scanning transmission electron microscopy, Ultramicroscopy **110**, 778 (2010).

[6] S. Van Aert, S. Turner, R. Delville, D. Schryvers, G. Van Tendeloo, and E. K. H. Salje, Direct observation of ferrielectricity at ferroelastic domain boundaries in CaTiO$_3$ by electron microscopy, Adv. Mater. **24**, 523 (2012).

[7] A. B. Yankovich, B. Berkels, W. Dahmen, P. Binev, S. I. Sanchez, S. A. Bradley, A. Li, I. Szlufarska, and P. M. Voyles, Picometre-precision analysis of scanning transmission electron microscopy images of platinum nanocatalysts, Nat. Commun. **5**, 4155 (2014).

[8] B. H. Savitzky, I. El Baggari, A. S. Admasu, J. Kim, S.-W. Cheong, R. Hovden, and L. F. Kourkoutis, Bending and breaking of stripes in a charge ordered manganite, Nat. Commun. **8**, 1883 (2017).

[9] M. E. Lines and A. M. Glass, *Principles and Applications of Ferroelectrics and Related Materials* (Oxford University Press, Oxford, 1977).

[10] A. K. Tagantsev, L. E. Cross, and J. Fousek, *Domains in Ferroic crystals and Thin Films* (Springer, New York, 2010).

[11] G. Catalan, J. Seidel, R. Ramesh, and J. F Scott, Domain wall nanoelectronics, Rev. Mod. Phys. **84**, 119 (2012).

[12] V. Gopalan, V. Dierolf, and D. A. Scrymgeour, Defect–domain wall interactions in trigonal ferroelectrics, Annu. Rev. Mater. Res. **37**, 449 (2007).

[13] E. A. Eliseev, A. N. Morozovska, G. S. Svechnikov, V. Gopalan, and V. Y. Shur, Static conductivity of charged domain walls in uniaxial ferroelectric semiconductors, Phys. Rev. B **83**, 235313 (2011).

[14] T. Sluka, A. K. Tagantsev, P. Bednyakov, and N. Setter, Free-electron gas at charged domain walls in insulating BaTiO$_3$, Nat. Commun. **4**, 1808 (2013).

[15] D. Lee, R. K. Behera, P. Wu, H. Xu, Y. L. Li, S. B. Sinnott, S. R. Phillpot, L. Q. Chen, and V. Gopalan, Mixed Bloch-Néel-Ising character of 180° ferroelectric domain walls, Phys. Rev. B **80**, 060102(R) (2009).

[16] Y. J. Wang, D. Chen, Y. L. Tang, Y. L. Zhu, and X. L. Ma, Origin of the Bloch-type polarization components at the 180° domain walls in ferroelectric PbTiO$_3$, J. Appl. Phys. **116**, 224105 (2014).

[17] X.-K. Wei, C.-L. Jia, T. Sluka, B.-X. Wang, Z.-G. Ye, and N. Setter, Néel-like domain walls in ferroelectric Pb(Zr, Ti)O$_3$ single crystals, Nat. Commun. **7**, 12385 (2016).

[18] J. C. Wojdeł and J. Iniguez, Ferroelectric Transitions at Ferroelectric Domain Walls Found from First Principles, Phys. Rev. Lett. **112**, 247603 (2014).

[19] T. Matsumoto, R. Ishikawa, T. Tohei, H. Kimura, Q. Yao, H. Zhao, X. Wang, D. Chen, Z. Cheng, N. Shibata *et al.*, Multivariate statistical characterization of charged and uncharged domain walls in multiferroic hexagonal YMnO$_3$ single crystal visualized by a spherical aberration-corrected stem, Nano Lett. **13**, 4594 (2013).

[20] Y.-M. Kim, S. J. Pennycook, and A. Y. Borisevich, Quantitative comparison of bright field and annular bright field imaging modes for characterization of oxygen octahedral tilts, Ultramicroscopy **181**, 1 (2017).

[21] Q. He, R. Ishikawa, A. R. Lupini, L. Qiao, E. J. Moon, O. Ovchinnikov, S. J. May, M. D. Biegalski, and A. Y. Borisevich, Towards 3D mapping of BO$_6$ octahedron rotations at perovskite heterointerfaces, unit cell by unit cell, ACS Nano **9**, 8412 (2015).

[22] T. Malis, S. C. Cheng, and R. F. Egerton, EELS log-ratio technique for specimen-thickness measurement in the TEM, J. Electron Microsc. Tech. **8**, 193 (1988).

[23] A. Jain, S. Ping Ong, G. Hautier, W. Chen, W. D. Richards, S. Dacek, S. Cholia, D. Gunter, D. Skinner, G. Ceder, and K. A. Persson, The Materials Project: A materials genome approach to accelerating materials innovation, APL Mater. **1**, 011002 (2013).

[24] J. Gonnissen, D. Batuk, G. F. Nataf, L. Jones, A. M. Abakumov, S. Van Aert, D. Schryvers, and E. K. H. Salje, Direct observation of ferroelectric domain walls in LiNbO$_3$: Wall-meanders, kinks, and local electric charges, Adv. Funct. Mater. **26**, 7599 (2016).

[25] D. A. Scrymgeour, V. Gopalan, A. Itagi, A. Saxena, and P. J. Swart, Phenomenological theory of a single domain wall in uniaxial trigonal ferroelectrics: Lithium niobate and lithium tantalate, Phys. Rev. B **71**, 184110 (2005).

[26] M. Veithen and Ph. Ghosez, First-principles study of the dielectric and dynamical properties of lithium niobate, Phys. Rev. B **65**, 214302 (2002).

[27] J. Goldstone, Field theories with superconductor solutions, Il Nuovo Cimento (1955-1965) **19**, 154 (1961).

[28] P. W. Higgs, Broken Symmetries and The Masses of Gauge Bosons, Phys. Rev. Lett. **13**, 508 (1964).

[29] P. Županović and D. Kuić, Relation between Boltzmann and Gibbs entropy and example with multinomial distribution, J. Phys. Commun. **2**, 045002 (2018).

[30] G. Stone, C. Ophus, T. Birol, J. Ciston, C.-H. Lee, K. Wang, C. J. Fennie, D. G Schlom, N. Alem, and V. Gopalan, Atomic scale imaging of competing polar states in

a Ruddlesden–Popper layered oxide, Nat. Commun. **7**, 12572 (2016).

[31] G. A. Smolenskii, N. N. Krainik, N. P. Khuchua, V. V. Zhdanova, and I. E. Mylnikova, The Curie Temperature of LiNbO₃, Phys. Status Solidi B **13**, 309 (1966).

[32] S. Kim, V. Gopalan, and A. Gruverman, Coercive fields in ferroelectrics: A case study in lithium niobate and lithium tantalate, Appl. Phys. Lett. **80**, 2740 (2002).

[33] H. F. Wang, Y. Y. Zhu, S. N. Zhu, and N. B. Ming, Investigation of ferroelectric coercive field in LiNbO₃, Appl. Phys. A: Mater. Sci. Process. **65**, 437 (1997).

[34] A. Filippetti, P. Delugas, M. I. Saba, and A. Mattoni, Entropy-suppressed ferroelectricity in hybrid lead-iodide perovskites, J. Phys. Chem. Lett. **6**, 4909 (2015).

[35] R. Pirc, B. Rožič, Z. Kutnjak, R. Blinc, X. Li, and Q. M. Zhang, Electrocaloric effect and dipolar entropy change in ferroelectric polymers, Ferroelectrics **426**, 38 (2012).

[36] G. G. Guzmán-Verri and P. B. Littlewood, Why is the electrocaloric effect so small in ferroelectrics? APL Mater. **4**, 064106 (2016).

[37] M. Porta, T. Lookman, and A. Saxena, Effects of criticality and disorder on piezoelectric properties of ferroelectrics, J. Phys.: Condens. Matter **22**, 345902 (2010).

[38] B. N. Rao, R. Datta, S. S. Chandrashekaran, D. K. Mishra, V. Sathe, A. Senyshyn, and R. Ranjan, Local structural disorder and its influence on the average global structure and polar properties in Na₀.₅Bi₀.₅TiO₃, Phys. Rev. B **88**, 224103 (2013).

[39] M. Schaffer, B. Schaffer, and Q. Ramasse, Sample preparation for atomic-resolution STEM at low voltages by FIB, Ultramicroscopy **114**, 62 (2012).

[40] L. A. Giannuzzi, Reducing FIB damage using low energy ions, Microsc. Microanal. **12**, 1260 (2006).

[41] J. Mayer, L. A. Giannuzzi, T. Kamino, and J. Michael, TEM sample preparation and FIB-induced damage, MRS Bull. **32**, 400 (2007).

[42] T. Grieb, M. Tewes, M. Schowalter, K. Müller-Caspary, F. F. Krause, T. Mehrtens, J.-M. Hartmann, and A. Rosenauer, Quantitative HAADF STEM of SiGe in presence of amorphous surface layers from FIB preparation, Ultramicroscopy **184**, 29 (2018).

[43] M. J. Zachman, Z. Tu, S. Choudhury, L. A. Archer, and L. F. Kourkoutis, Cryo-STEM mapping of solid–liquid interfaces and dendrites in lithium-metal batteries, Nature (London) **560**, 345 (2018).

[44] C. Ophus, J. Ciston, and C. T. Nelson, Correcting nonlinear drift distortion of scanning probe and scanning transmission electron microscopies from image pairs with orthogonal scan directions, Ultramicroscopy **162**, 1 (2016).

[45] O. Tikhomirov, H. Jiang, and J. Levy, Local Ferroelectricity in SrTiO₃ Thin Films, Phys. Rev. Lett. **89**, 147601 (2002).

[46] S. C. Abrahams, J. M. Reddy, and J. L. Bernstein, Ferroelectric lithium niobate. 3. single crystal x-ray diffraction study at 24°C, J. Phys. Chem. Solids **27**, 997 (1966).

[47] W. H. Richardson, Bayesian-based iterative method of image restoration, J. Opt. Soc. Am. **62**, 55 (1972).

[48] L. B. Lucy, An iterative technique for the rectification of observed distributions, Astron. J. **79**, 745 (1974).

[49] X. Gonze, F. Jollet, F. A. Araujo, D. Adams, B. Amadon, T. Applencourt, C. Audouze, J.-M. Beuken, J. Bieder, A. Bokhanchuk *et al.*, Recent developments in the ABINIT software package, Comput. Phys. Commun. **205**, 106 (2016).

[50] E. K. U. Gross and R. M. Dreizler, *Density Functional Theory*, Vol. 337 (Springer, New York, 2013).

[51] P. Hohenberg and W. Kohn, Inhomogeneous electron gas, Phys. Rev. **136**, B864 (1964).

[52] X. Gonze, B. Amadon, P.-M. Anglade, J.-M. Beuken, F. Bottin, P. Boulanger, F. Bruneval, D. Caliste, R. Caracas, M. Côté *et al.*, ABINIT: First-principles approach to material and nanosystem properties, Comput. Phys. Commun. **180**, 2582 (2009).

[53] J. P. Perdew, A. Ruzsinszky, G. I. Csonka, O. A. Vydrov, G. E. Scuseria, L. A. Constantin, X. Zhou, and K. Burke, Restoring the Density-Gradient Expansion for Exchange in Solids and Surfaces, Phys. Rev. Lett. **100**, 136406 (2008).

[54] M. A. L. Marques, M. J. T. Oliveira, and T. Burnus, Libxc: A library of exchange and correlation functionals for density functional theory, Comput. Phys. Commun. **183**, 2272 (2012).

[55] M. van Setten, M. Giantomassi, E. Bousquet, M. J. Verstraete, D. R. Hamann, X. Gonze, and G.-M. Rignanese, The PseudoDojo: Training and grading a 85 element optimized norm-conserving pseudopotential table, Comput. Phys. Commun. **226**, 39 (2018).

[56] D. R. Hamann, Optimized norm-conserving Vanderbilt pseudopotentials, Phys. Rev. B **88**, 085117 (2013).

[57] F. Casas, A. Murua, and M. Nadinic, Efficient computation of the Zassenhaus formula, Comput. Phys. Commun. **183**, 2386 (2012).

[58] H. J. Monkhorst and J. D. Pack, Special points for brillouin-zone integrations, Phys. Rev. B **13**, 5188 (1976).

[59] I. Tomeno and S. Matsumura, Elastic and dielectric properties of LiNbO₃, J. Phys. Soc. Jpn. **56**, 163 (1987).

[60] H. Boysen and F. Altorfer, A neutron powder investigation of the high-temperature structure and phase transition in LiNbO₃, Acta Crystallogr., Sect. B: Struct. Sci. **50**, 405 (1994).

[61] H. D. Megaw, A note on the structure of lithium niobate, LiNbO₃, Acta Crystallogr., Sect. A **24**, 583 (1968).

[62] M. A. O'Keefe and R. Kilaas, Advances in high-resolution image simulation, Scanning Microsc. Suppl. **2**, 225 (1988).